Applied Superconductivity:

Josephson Effect and Superconducting Electronics

Manuscript to the Lectures during WS 2003/2004, WS 2005/2006, WS 2006/2007, WS 2007/2008, WS 2008/2009, and WS 2009/2010

Prof. Dr. Rudolf Gross
and
Dr. Achim Marx

Walther-Meißner-Institut
Bayerische Akademie der Wissenschaften
and
Lehrstuhl für Technische Physik (E23)
Technische Universität München

Walther-Meißner-Strasse 8
D-85748 Garching
Rudolf.Gross@wmi.badw.de

© Walther-Meißner-Institut — Garching, October 2005

Contents

Preface **xxi**

I Foundations of the Josephson Effect **1**

1 Macroscopic Quantum Phenomena **3**

1.1 The Macroscopic Quantum Model . . . 3
  1.1.1 Coherent Phenomena in Superconductivity . . . 3
  1.1.2 Macroscopic Quantum Currents in Superconductors . . . 12
  1.1.3 The London Equations . . . 18
1.2 Flux Quantization . . . 24
  1.2.1 Flux and Fluxoid Quantization . . . 26
  1.2.2 Experimental Proof of Flux Quantization . . . 28
  1.2.3 Additional Topic: Rotating Superconductor . . . 30
1.3 Josephson Effect . . . 32
  1.3.1 The Josephson Equations . . . 33
  1.3.2 Josephson Tunneling . . . 37

2 JJs: The Zero Voltage State **43**

2.1 Basic Properties of Lumped Josephson Junctions . . . 44
  2.1.1 The Lumped Josephson Junction . . . 44
  2.1.2 The Josephson Coupling Energy . . . 45
  2.1.3 The Superconducting State . . . 47
  2.1.4 The Josephson Inductance . . . 49
  2.1.5 Mechanical Analogs . . . 49
2.2 Short Josephson Junctions . . . 50
  2.2.1 Quantum Interference Effects – Short Josephson Junction in an Applied Magnetic Field . . . 50

2.2.2 The Fraunhofer Diffraction Pattern 54

2.2.3 Determination of the Maximum Josephson Current Density 58

2.2.4 Additional Topic:
Direct Imaging of the Supercurrent Distribution 62

2.2.5 Additional Topic:
Short Josephson Junctions: Energy Considerations 63

2.2.6 The Motion of Josephson Vortices 65

2.3 Long Josephson Junctions 68

2.3.1 The Stationary Sine-Gordon Equation 68

2.3.2 The Josephson Vortex 70

2.3.3 Junction Types and Boundary Conditions 73

2.3.4 Additional Topic:
Josephson Current Density Distribution and Maximum Josephson Current 79

2.3.5 The Pendulum Analog 84

3 JJs: The Voltage State 89

3.1 The Basic Equation of the Lumped Josephson Junction 90

3.1.1 The Normal Current: Junction Resistance 90

3.1.2 The Displacement Current: Junction Capacitance 92

3.1.3 Characteristic Times and Frequencies 93

3.1.4 The Fluctuation Current 94

3.1.5 The Basic Junction Equation 96

3.2 The Resistively and Capacitively Shunted Junction Model 97

3.2.1 Underdamped and Overdamped Josephson Junctions 100

3.3 Response to Driving Sources 102

3.3.1 Response to a dc Current Source 102

3.3.2 Response to a dc Voltage Source 107

3.3.3 Response to ac Driving Sources 107

3.3.4 Photon-Assisted Tunneling 112

3.4 Additional Topic:
Effect of Thermal Fluctuations 115

3.4.1 Underdamped Junctions: Reduction of I_c by Premature Switching 117

3.4.2 Overdamped Junctions: The Ambegaokar-Halperin Theory 118

3.5 Secondary Quantum Macroscopic Effects 122

3.5.1 Quantum Consequences of the Small Junction Capacitance 122

3.5.2 Limiting Cases: The Phase and Charge Regime 125
3.5.3 Coulomb and Flux Blockade 128
3.5.4 Coherent Charge and Phase States 130
3.5.5 Quantum Fluctuations 132
3.5.6 Macroscopic Quantum Tunneling 133
3.6 Voltage State of Extended Josephson Junctions 139
3.6.1 Negligible Screening Effects 139
3.6.2 The Time Dependent Sine-Gordon Equation 140
3.6.3 Solutions of the Time Dependent Sine-Gordon Equation 141
3.6.4 Additional Topic: Resonance Phenomena 144

II Applications of the Josephson Effect 153

4 SQUIDs 157
4.1 The dc-SQUID 159
4.1.1 The Zero Voltage State 159
4.1.2 The Voltage State 164
4.1.3 Operation and Performance of dc-SQUIDs 168
4.1.4 Practical dc-SQUIDs 172
4.1.5 Read-Out Schemes 176
4.2 Additional Topic: The rf-SQUID 180
4.2.1 The Zero Voltage State 180
4.2.2 Operation and Performance of rf-SQUIDs 182
4.2.3 Practical rf-SQUIDs 186
4.3 Additional Topic: Other SQUID Configurations 188
4.3.1 The DROS 188
4.3.2 The SQIF 189
4.3.3 Cartwheel SQUID 189
4.4 Instruments Based on SQUIDs 191
4.4.1 Magnetometers 192
4.4.2 Gradiometers 194
4.4.3 Susceptometers 196

4.4.4 Voltmeters 197
4.4.5 Radiofrequency Amplifiers 198
4.5 Applications of SQUIDs 200
4.5.1 Biomagnetism 200
4.5.2 Nondestructive Evaluation 204
4.5.3 SQUID Microscopy 206
4.5.4 Gravity Wave Antennas and Gravity Gradiometers 208
4.5.5 Geophysics 210

5 Digital Electronics 215
5.1 Superconductivity and Digital Electronics 216
5.1.1 Historical development 217
5.1.2 Advantages and Disadvantages of Josephson Switching Devices 219
5.2 Voltage State Josephson Logic 222
5.2.1 Operation Principle and Switching Times 222
5.2.2 Power Dissipation 225
5.2.3 Switching Dynamics, Global Clock and Punchthrough 226
5.2.4 Josephson Logic Gates 228
5.2.5 Memory Cells 234
5.2.6 Microprocessors 236
5.2.7 Problems of Josephson Logic Gates 237
5.3 RSFQ Logic 239
5.3.1 Basic Components of RSFQ Circuits 241
5.3.2 Information in RSFQ Circuits 246
5.3.3 Basic Logic Gates 247
5.3.4 Timing and Power Supply 249
5.3.5 Maximum Speed 249
5.3.6 Power Dissipation 250
5.3.7 Prospects of RSFQ 250
5.3.8 Fabrication Technology 253
5.3.9 RSFQ Roadmap 254
5.4 Analog-to-Digital Converters 255
5.4.1 Additional Topic:
Foundations of ADCs 256
5.4.2 The Comparator 261
5.4.3 The Aperture Time 263
5.4.4 Different Types of ADCs 264

6 The Josephson Voltage Standard 269

6.1 Voltage Standards 270

6.1.1 Standard Cells and Electrical Standards 270

6.1.2 Quantum Standards for Electrical Units 271

6.2 The Josephson Voltage Standard 274

6.2.1 Underlying Physics 274

6.2.2 Development of the Josephson Voltage Standard 274

6.2.3 Junction and Circuit Parameters for Series Arrays 279

6.3 Programmable Josephson Voltage Standard 281

6.3.1 Pulse Driven Josephson Arrays 283

7 Superconducting Photon and Particle Detectors 285

7.1 Superconducting Microwave Detectors: Heterodyne Receivers 286

7.1.1 Noise Equivalent Power and Noise Temperature 286

7.1.2 Operation Principle of Mixers 287

7.1.3 Noise Temperature of Heterodyne Receivers 290

7.1.4 SIS Quasiparticle Mixers 292

7.1.5 Josephson Mixers 296

7.2 Superconducting Microwave Detectors: Direct Detectors 297

7.2.1 NEP of Direct Detectors 298

7.3 Thermal Detectors 300

7.3.1 Principle of Thermal Detection 300

7.3.2 Bolometers 302

7.3.3 Antenna-Coupled Microbolometers 307

7.4 Superconducting Particle and Single Photon Detectors 314

7.4.1 Thermal Photon and Particle Detectors: Microcalorimeters 314

7.4.2 Superconducting Tunnel Junction Photon and Particle Detectors 318

7.5 Other Detectors 328

8 Microwave Applications 329

8.1 High Frequency Properties of Superconductors 330

8.1.1 The Two-Fluid Model 330

8.1.2 The Surface Impedance 333

8.2 Superconducting Resonators and Filters 336

8.3 Superconducting Microwave Sources 337

9 Superconducting Quantum Bits **339**
- 9.1 Quantum Bits and Quantum Computers 341
  - 9.1.1 Quantum Bits 341
  - 9.1.2 Quantum Computing 343
  - 9.1.3 Quantum Error Correction 346
  - 9.1.4 What are the Problems? 348
- 9.2 Implementation of Quantum Bits 349
- 9.3 Why Superconducting Qubits 352
  - 9.3.1 Superconducting Island with Leads 352

III Anhang **355**

A The Josephson Equations **357**

B Imaging of the Maximum Josephson Current Density **361**

C Numerical Iteration Method for the Calculation of the Josephson Current Distribution **363**

D Photon Noise **365**
- I Power of Blackbody Radiation 365
- II Noise Equivalent Power 367

E Qubits **369**
- I What is a quantum bit ? 369
  - I.1 Single-Qubit Systems 369
  - I.2 The spin-1/2 system 371
  - I.3 Two-Qubit Systems 372
- II Entanglement 373
- III Qubit Operations 375
  - III.1 Unitarity 375
  - III.2 Single Qubit Operations 375
  - III.3 Two Qubit Operations 376
- IV Quantum Logic Gates 377
  - IV.1 Single-Bit Gates 377
  - IV.2 Two Bit Gates 379
- V The No-Cloning Theorem 384
- VI Quantum Complexity 385
- VII The Density Matrix Representation 385

F Two-Level Systems 389

I Introduction to the Problem 389

I.1 Relation to Spin-1/2 Systems 390

II Static Properties of Two-Level Systems 390

II.1 Eigenstates and Eigenvalues 390

II.2 Interpretation 391

II.3 Quantum Resonance 394

III Dynamic Properties of Two-Level Systems 395

III.1 Time Evolution of the State Vector 395

III.2 The Rabi Formula 395

G The Spin 1/2 System 399

I Experimental Demonstration of Angular Momentum Quantization 399

II Theoretical Description 401

II.1 The Spin Space 401

III Evolution of a Spin 1/2 Particle in a Homogeneous Magnetic Field 402

IV Spin 1/2 Particle in a Rotating Magnetic Field 404

IV.1 Classical Treatment 404

IV.2 Quantum Mechanical Treatment 406

IV.3 Rabi's Formula 407

H Literature 409

I Foundations of Superconductivity 409

I.1 Introduction to Superconductivity 409

I.2 Early Work on Superconductivity and Superfluidity 410

I.3 History of Superconductivity 410

I.4 Weak Superconductivity, Josephson Effect, Flux Structures 410

II Applications of Superconductivity 411

II.1 Electronics, Sensors, Microwave Devices 411

II.2 Power Applications, Magnets, Transportation 412

II.3 Superconducting Materials 412

I SI-Einheiten 413

I Geschichte des SI Systems 413

II Die SI Basiseinheiten 415

III Einige von den SI Einheiten abgeleitete Einheiten 416

IV Vorsätze 418

V Abgeleitete Einheiten und Umrechnungsfaktoren 419

J Physikalische Konstanten **425**

List of Figures

1.1 Meissner-Effect 19

1.2 Current transport and decay of a supercurrent in the Fermi sphere picture 20

1.3 Stationary Quantum States 24

1.4 Flux Quantization in Superconductors 25

1.5 Flux Quantization in a Superconducting Cylinder 27

1.6 Experiment by Doll and Naebauer 29

1.7 Experimental Proof of Flux Quantization 29

1.8 Rotating superconducting cylinder 31

1.9 The Josephson Effect in weakly coupled superconductors 32

1.10 Variation of $n_s^\star$ and γ across a Josephson junction 35

1.11 Schematic View of a Josephson Junction 36

1.12 Josephson Tunneling 39

2.1 Lumped Josephson Junction 45

2.2 Coupling Energy and Josephson Current 46

2.3 The Tilted Washboard Potential 48

2.4 Extended Josephson Junction 51

2.5 Magnetic Field Dependence of the Maximum Josephson Current 55

2.6 Josephson Current Distribution in a Small Josephson Junction for Various Applied Magnetic Fields 56

2.7 Spatial Interference of Macroscopic Wave Funktions 57

2.8 The Josephson Vortex 57

2.9 Gaussian Shaped Josephson Junction 59

2.10 Comparison between Measurement of Maximum Josephson Current and Optical Diffraction Experiment 60

2.11 Supercurrent Auto-correlation Function 61

2.12 Magnetic Field Dependence of the Maximum Josephson Current of a YBCO-GBJ 63

2.13 Motion of Josephson Vortices 66

2.14 Magnetic Flux and Current Density Distribution for a Josephson Vortex 70

2.15 Classification of Junction Types: Overlap, Inline and Grain Boundary Junction 74

2.16 Geometry of the Asymmetric Inline Junction 77

2.17 Geometry of Mixed Overlap and Inline Junctions 78

2.18 The Josephson Current Distribution of a Long Inline Junction 80

2.19 The Maximum Josephson Current as a Function of the Junction Length 81

2.20 Magnetic Field Dependence of the Maximum Josephson Current and the Josephson Current Density Distribution in an Overlap Junction 83

2.21 The Maximum Josephson Current as a Function of the Applied Field for Overlap and Inline Junctions 84

3.1 Current-Voltage Characteristic of a Josephson tunnel junction 91

3.2 Equivalent circuit for a Josephson junction including the normal, displacement and fluctuation current 92

3.3 Equivalent circuit of the Resistively Shunted Junction Model 97

3.4 The Motion of a Particle in the Tilt Washboard Potential 98

3.5 Pendulum analogue of a Josephson junction 99

3.6 The IVCs for Underdamped and Overdamped Josephson Junctions 101

3.7 The time variation of the junction voltage and the Josephson current 103

3.8 The RSJ model current-voltage characteristics 105

3.9 The RCSJ Model IVC at Intermediate Damping 107

3.10 The RCJ Model Circuit for an Applied dc and ac Voltage Source 108

3.11 Overdamped Josephson Junction driven by a dc and ac Voltage Source 110

3.12 Overdamped Josephson junction driven by a dc and ac Current Source 111

3.13 Shapiro steps for under- and overdamped Josephson junction 112

3.14 Photon assisted tunneling 113

3.15 Photon assisted tunneling in SIS Josephson junction 113

3.16 Thermally Activated Phase Slippage 116

3.17 Temperature Dependence of the Thermally Activated Junction Resistance 119

3.18 RSJ Model Current-Voltage Characteristics Including Thermally Activated Phase Slippage 120

3.19 Variation of the Josephson Coupling Energy and the Charging Energy with the Junction Area 124

3.20 Energy diagrams of an isolated Josephson junction 127

3.21 The Coulomb Blockade 128

3.22 The Phase Blockade 129

3.23 The Cooper pair box 131

3.24 Double well potential for the generation of phase superposition states 132

3.25 Macroscopic Quantum Tunneling 134

3.26 Macroscopic Quantum Tunneling at Large Damping 138

3.27 Mechanical analogue for phase dynamics of a long Josephson junction 141

3.28 The Current Voltage Characteristic of an Underdamped Long Josephson Junction 145

3.29 Zero field steps in IVCs of an annular Josephson junction 147

4.1 The dc-SQUID 160

4.2 Maximum Supercurrent versus Applied Magnetic Flux for a dc-SQUID at Weak Screening 162

4.3 Total Flux versus Applied Magnetic Flux for a dc SQUID at $\beta_L > 1$ 163

4.4 Current-voltage Characteristics of a dc-SQUID at Negligible Screening 165

4.5 The pendulum analogue of a dc SQUID 167

4.6 Principle of Operation of a dc-SQUID 169

4.7 Energy Resolution of dc-SQUIDs 172

4.8 The Practical dc-SQUID 173

4.9 Geometries for thin film SQUID washers 174

4.10 Flux focusing effect in a $YBa_2Cu_3O_{7-\delta}$ washer 175

4.11 The Washer dc-SQUID 176

4.12 The Flux Modulation Scheme for a dc-SQUID 177

4.13 The Modulation and Feedback Circuit of a dc-SQUID 178

4.14 The rf-SQUID 180

4.15 Total flux versus applied flux for a rf-SQUID 182

4.16 Operation of rf-SQUIDs 183

4.17 Tank voltage versus rf-current for a rf-SQUID 184

4.18 High T_c rf-SQUID 187

4.19 The double relaxation oscillation SQUID (DROS) 188

4.20 The Superconducting Quantum Interference Filter (SQIF) 190

4.21 Input Antenna for SQUIDs 191

4.22 Various types of thin film SQUID magnetometers 193

4.23 Magnetic noise signals 194

4.24 Magnetically shielded room 195

4.25 Various gradiometers configurations 196

4.26 Miniature SQUID Susceptometer . . . 197
4.27 SQUID Radio-frequency Amplifier . . . 198
4.28 Multichannel SQUID Systems . . . 201
4.29 Magnetocardiography . . . 203
4.30 Magnetic field distribution during R peak . . . 204
4.31 SQUID based nondestructive evaluation . . . 205
4.32 Scanning SQUID microscopy . . . 207
4.33 Scanning SQUID microscopy images . . . 208
4.34 Gravity wave antenna . . . 209
4.35 Gravity gradiometer . . . 210

5.1 Cryotron . . . 217
5.2 Josephson Cryotron . . . 218
5.3 Device performance of Josephson devices . . . 220
5.4 Principle of operation of a Josephson switching device . . . 222
5.5 Output current of a Josephson switching device . . . 224
5.6 Threshold characteristics for a magnetically and directly coupled gate . . . 229
5.7 Three-junction interferometer gate . . . 230
5.8 Current injection device . . . 230
5.9 Josephson Atto Weber Switch (JAWS) . . . 231
5.10 Direct coupled logic (DCL) gate . . . 231
5.11 Resistor coupled logic (RCL) gate . . . 232
5.12 4 junction logic (4JL) gate . . . 232
5.13 Non-destructive readout memory cell . . . 234
5.14 Destructive read-out memory cell . . . 235
5.15 4 bit Josephson microprocessor . . . 237
5.16 Josephson microprocessor . . . 238
5.17 Comparison of latching and non-latching Josephson logic . . . 240
5.18 Generation of SFQ Pulses . . . 242
5.19 dc to SFQ Converter . . . 243
5.20 Basic Elements of RSFQ Circuits . . . 244
5.21 RSFQ memory cell . . . 245
5.22 RSFQ logic . . . 246
5.23 RSFQ OR and AND Gate . . . 247

5.24 RSFQ NOT Gate 248
5.25 RSFQ Shift Register 249
5.26 RSFQ Microprocessor 253
5.27 RSFQ roadmap 254
5.28 Principle of operation of an analog-to-digital converter 256
5.29 Analog-to-Digital Conversion 257
5.30 Semiconductor and Superconductor Comparators 262
5.31 Incremental Quantizer 263
5.32 Flash-type ADC 265
5.33 Counting-type ADC 266

6.1 Weston cell 271
6.2 The metrological triangle for the electrical units 273
6.3 IVC of an underdamped Josephson junction under microwave irradiation 275
6.4 International voltage comparison between 1920 and 2000 276
6.5 One-Volt Josephson junction array 277
6.6 Josephson series array embedded into microwave stripline 278
6.7 Microwave design of Josephson voltage standards 279
6.8 Adjustment of Shapiro steps for a series array Josephson voltage standard 281
6.9 IVC of overdamped Josephson junction with microwave irradiation 282
6.10 Programmable Josephson voltage standard 283

7.1 Block diagram of a heterodyne receiver 288
7.2 Ideal mixer as a switch 288
7.3 Current response of a heterodyne mixer 289
7.4 IVCs and IF output power of SIS mixer 290
7.5 Optimum noise temperature of a SIS quasiparticle mixer 293
7.6 Measured DSB noise temperature of a SIS quasiparticle mixers 294
7.7 High frequency coupling schemes for SIS mixers 295
7.8 Principle of thermal detectors 301
7.9 Operation principle of superconducting transition edge bolometer 302
7.10 Sketch of a HTS bolometer 305
7.11 Specific detectivity of various bolometers 305
7.12 Relaxation processes in a superconductor after energy absorption 307
7.13 Antenna-coupled microbolometer 308

7.14 Schematic illustration of the hot electron bolometer mixer . . . 309
7.15 Hot electron bolometer mixers with different antenna structures . . . 311
7.16 Transition-edge sensors . . . 315
7.17 Transition-edge sensors . . . 317
7.18 Functional principle of a superconducting tunnel junction detector . . . 319
7.19 Circuit diagram of a superconducting tunnel junction detector . . . 319
7.20 Energy resolving power of STJDs . . . 321
7.21 Quasiparticle tunneling in SIS junctions . . . 323
7.22 Quasiparticle trapping in STJDs . . . 326
7.23 STJDs employing lateral quasiparticle trapping . . . 326
7.24 Superconducting tunnel junction x-ray detector . . . 327

8.1 Equivalent circuit for the two-fluid model . . . 332
8.2 Characteristic frequency regimes for a superconductor . . . 332
8.3 Surface resistance of Nb and Cu . . . 335

9.1 Konrad Zuse 1945 . . . 341
9.2 Representation of a Qubit State as a Vector on the Bloch Sphere . . . 342
9.3 Operational Scheme of a Quantum Computer . . . 344
9.4 Quantum Computing: What's it good for? . . . 345
9.5 Shor, Feynman, Bennett and Deutsch . . . 346
9.6 Qubit Realization by Quantum Mechanical Two level System . . . 349
9.7 Use of Superconductors for Qubits . . . 352
9.8 Superconducting Island with Leads . . . 354

E.1 The Bloch Sphere S^2 . . . 370
E.2 The Spin-1/2 System . . . 371
E.3 Entanglement – an artist's view. . . . 373
E.4 Classical Single-Bit Gate . . . 377
E.5 Quantum NOT Gate . . . 378
E.6 Classical Two Bit Gate . . . 380
E.7 Reversible and Irreversible Logic . . . 380
E.8 Reversible Classical Logic . . . 381
E.9 Reversible XOR (CNOT) and SWAP Gate . . . 382
E.10 The Controlled U Gate . . . 382

E.11 Density Matrix for Pure Single Qubit States 386
E.12 Density Matrix for a Coherent Superposition of Single Qubit States 387

F.1 Energy Levels of a Two-Level System 392
F.2 The Benzene Molecule 394
F.3 Graphical Representation of the Rabi Formula 396

G.1 The Larmor Precession 400
G.2 The Rotating Reference Frame 404
G.3 The Effective Magnetic Field in the Rotating Reference Frame 405
G.4 Rabi's Formula for a Spin 1/2 System 408

List of Tables

5.1 Switching delay and power dissipation for various types of logic gates. 233
5.2 Josephson 4 kbit RAM characteristics (organization: 4096 word x 1 bit, NEC). 236
5.3 Performance of various logic gates 237
5.4 Possible applications of superconductor digital circuits (source: SCENET 2001). 251
5.5 Performance of various RSFQ based circuits. 252

7.1 Characteristic materials properties of some superconductors 325

8.1 Important high-frequency characteristic of superconducting and normal conducting . . . 334

E.1 Successive measurements on a two-qubit state showing the results A and B with the corresponding probabilities $P(A)$ and $P(B)$ and the remaining state after the measurement. . . . 373

Chapter 7

Superconducting Photon and Particle Detectors

Superconducting devices can be used for the sensitive detection of various quantities. We already have seen in Chapter 4 that SQUIDs can be used for the detection of magnetic flux at an accuracy below $10^{-6}\Phi_0$ and all other quantities that can be converted into a magnetic flux signal using a suitable antenna structure. In this Chapter we discuss the application of Josephson junctions as detectors for photons ranging from the microwave to the x-ray regime as well as for particles such as electrons, atoms, molecules etc.. With respect to the detection of microwave radiation the detection principle is based on the interaction of the microwave signal with the Josephson current resulting in Shapiro steps or the photon assisted tunneling process of quasiparticles. For radiation in the optical to x-ray regime both thermal detectors and nonthermal detector are used. The former are based on the sensitive measurement of the temperature rise induced by the incident radiation making use of the strong temperature dependence of the resistance or inductance of a superconducting thin film. The latter are based on the counting of excess quasiparticles generated in a superconductor due to the absorption of photons or particles.

In general, superconducting detectors can be classified in the following three categories

detector class	range	f_s (Hz)	λ (μm)	example	mechanism
modulation	radio, microwave	$< 10^{12}$	> 1000	heterodyne detector, direct detector	coherent incoherent
thermal	infrared	$10^{11} - 10^{15}$	$1 - 1000$	bolometer	incoherent
photon	visible, UV, x-ray	$> 10^{14}$	< 1	tunnel junction photon detector	incoherent

In the low frequency regime up to microwave frequencies, a ***modulation detector*** is fast enough to follow the incoming electromagnetic signal directly. In the intermediate regime, typically the infrared regime, the detector can no longer follow the signal directly so that modulation detectors do not work. Furthermore, the photon energy is too small to allow single photon detection. In this regime often ***thermal detectors*** are used, which measure the thermal response due to a larger number of absorbed photons. In the high frequency regime, typically from the visible to the x-ray regime, the detector is sensitive enough to measure the response due to the absorption of a single photon or particle. In this regime superconducting detectors can be used as single photon or particle detectors.

7.1 Superconducting Microwave Detectors: Heterodyne Receivers

Heterodyne receivers are modulation detectors used for the detection of high frequency signals in telecommunication systems and microwave instrumentation ranging from the radio to the mobile phone, television and satellite systems. The high frequency signal to be received is mixed with a so-called local oscillator signal thereby generating an intermediate frequency signal at the much lower difference frequency, which is processed further. One distinguishes between the ***heterodyne receiver***, where the signal frequency f_s and the local oscillator frequency $f_{\rm lo}$ are different and the ***homodyne receiver***, where f_s and $f_{\rm lo}$ are the same.

The development of low-noise superconducting heterodyne receivers was strongly stimulated by radio astronomy dealing with the observation of molecules and atoms in interstellar clouds. Most molecules are observed through their rotational emission lines. After the discovery of the spectral emission of carbon monoxide in 1970,[1] millimeter-wave radio astronomy became one of the most important branches of observational astronomy. Usually the associated signals are very weak corresponding about 10^6 microwave photons per second in a frequency interval of several 10 MHz. For the electronic processing of such weak signals with frequencies ranging from about 100 GHz to several THz amplifiers with sufficiently low noise temperatures do not exist. Therefore, heterodyne receivers have to be used for signal detection. Here, due to their superior noise performance receivers based on superconducting mixers play a dominating role.[2,3,4]

7.1.1 Noise Equivalent Power and Noise Temperature

Before discussing the functional principle of superconducting heterodyne receivers, we introduce the quantities ***Noise Equivalent Power (NEP)*** and ***noise temperature*** T_N of detectors. As already discussed in Chapter 3, there are various sources of fluctuations of physical quantities that can be characterized by a noise power spectral density $S(f)$. Depending on the frequency dependence and the physical origin of the noise we distinguish between ***Nyquist noise*** and ***shot noise*** with white frequency spectrum, or ***1/f noise*** (cf. section 3.1.4).

In order to detect a signal, the ***signal-to-noise ratio (SNR)*** must be larger than one, that is, the signal has to be larger than the noise floor. In this context, one can define the NEP of a detector as the equivalent signal power resulting in a SNR of one. That is, the NEP is equivalent to the signal power within a bandwidth $B = 1$ Hz, which generates the same signal in the detector as the noise within the same bandwidth. In order to give an example we consider a detector, in which an incident signal power P_s generates a current response I_s. If the current noise power spectral density of this detector is $S_I(f) = \langle \Delta I^2 \rangle / \mathrm{B}$, then the NEP in W/$\sqrt{\mathrm{Hz}}$ can be written as

$$\boxed{\mathrm{NEP} \;=\; \sqrt{S_I(f)}\,\frac{P_s}{I_s} \;=\; \sqrt{\frac{\langle \Delta I^2 \rangle}{B}}\,\frac{P_s}{I_s}\;.} \tag{7.1.1}$$

---

[1] R.W. Wilson, K.B. Jefferts, A.A. Penzias, *Carbon monoxide in the Orion nebula*, Astrophysics J. **116**, L43 (1970).

[2] J.E. Carlstrom, J. Zmuidzinas, *Millimeter and sub-millimeter techniques*, Reviews of Radio Sciences **1993-1995**, W.R. Stone ed., Oxford University Press, Oxford (1996).

[3] R. Blundell and C.-Y. E. Tong, *Sub-millimeter receivers for radio astronomy*, Proc. IEEE **80**, 1702 (1992).

[4] T. Noguchi, S.-C. Shi, *Superconducting heterodyne receivers*, Handbook of Applied Superconductivity Vol. 2, B. Seeber ed., Institute of Physics Publishing, Bristol (1998).

We can divide the NEP by Boltzmann's constant and $\sqrt{B}$ to obtain the noise temperature

$$\boxed{T_N \;=\; \sqrt{\frac{S_I(f)}{B}}\,\frac{P_s}{k_B I_s} \;=\; \frac{\sqrt{\langle \Delta I^2\rangle}}{B}\,\frac{P_s}{k_B I_s}\;.} \tag{7.1.2}$$

A further common quantity is the ***detectivity*** $D = 1/\mathrm{NEP}$ or the ***specific detectivity*** $D^\star = D/\sqrt{A}$, where A is the detector area. In order to compare different detectors often the energy resolution in units of J/Hz is used. This quantity we already have used to characterize SQUID detectors in Chapter 4. It gives the energy per bandwidth of 1 Hz, which is associated with the detector noise.

Quantum Limit

In the ideal case the energy resolution or the noise temperature are limited only by quantum fluctuations, which can be obtained from quantization of the external circuit. The energy resolution or noise temperature due to quantum fluctuations represents the limiting value that can be reached under optimum conditions. According to (3.5.28) the average energy $E(\omega,T)$ of a quantum oscillator with frequency ω at temperature T is

$$E(\omega,T) \;=\; \frac{P_N^{\mathrm{q}}}{B} \;=\; \frac{\hbar\omega}{2}\coth\left(\frac{\hbar\omega}{2k_BT}\right)\;. \tag{7.1.3}$$

At $T = 0$ this gives a minimum noise power $\hbar\omega B/2$ due to quantum fluctuations. We now can define a noise temperature T_N^{q} by setting $\hbar\omega B/2$ equal to $k_B T_N^{\mathrm{q}} B$. This results in[5]

$$\boxed{T_N^{\mathrm{q}} \;=\; \frac{\hbar\omega}{2k_B} = \frac{hf}{2k_B}\;.} \tag{7.1.4}$$

Putting in numbers we obtain $T_N^{\mathrm{q}} \simeq 0.025$ K/GHz, i.e. a quantum limited noise temperature of about 2.5 K at $f = 100$ GHz.

7.1.2 Operation Principle of Mixers

The operation principle of a heterodyne receiver is shown in Fig. 7.1. The key element of a heterodyne receiver is a frequency mixer, which is a nonlinear circuit or device (e.g. a Schottky diode or a Josephson junction) which mixes the weak (e.g. astronomical) signal at the frequency f_s with a stronger signal from a local oscillator (LO) at the frequency f_{lo}. The resulting intermediate frequency (IF) $f_{\mathrm{IF}} = |f_s - f_{\mathrm{lo}}|$ is amplified by a broadband IF amplifier within a bandwidth Δf_{IF} of typically less than 1 GHz around a center frequency typically ranging between 1.5 and 4 GHz. For this frequency regime amplifiers with noise temperatures below 10 K are available. The output of the IF amplifier is then analyzed by a spectrum analyzer or a filter spectrometer. The resulting spectrum obtains information on the signal in a frequency range determined by the bandwidth of the IF amplifier.

---

[5] This result also can be obtained by the following qualitative arguments: If we are measuring a signal for the period $\tau = 1/\Delta f$, according to the energy-time uncertainty relation the energy uncertainty must be at least $\Delta E/\Delta f = \hbar/2$. If we are detecting a radiation field of frequency ω within this bandwidth, this corresponds to minimum noise energy of $\hbar\omega/2$.

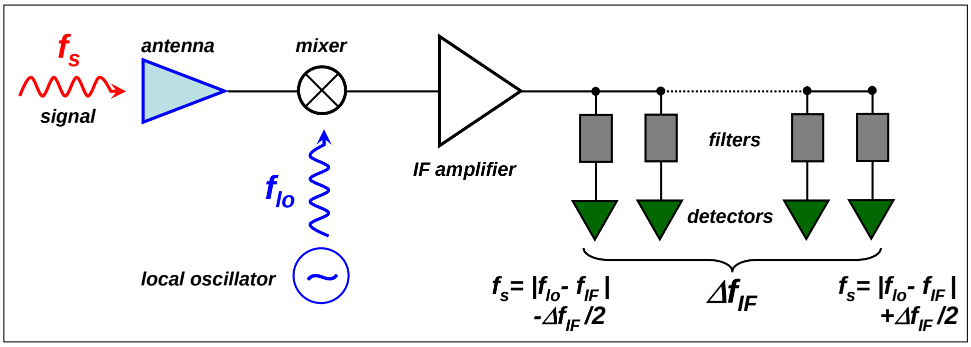

Figure 7.1: Block diagram of a heterodyne receiver with a backend filter spectrometer.

An ideal mixer consists of a switch that can be opened and closed at frequency f_{lo} without dissipation. Then, as it is evident from the equivalent circuit shown in Fig. 7.2a, we obtain a signal at the intermediate frequency $f_{\mathrm{IF}} = |f_s - f_{\mathrm{lo}}|$. This phenomenon is well known from the stroboscopic illumination at frequency f_{lo} of an object rotating at frequency f_s. Of course, for a proper operation of the mixer the closing period of the switch must be smaller than $1/f_{\mathrm{lo}}$. That is, a very fast switch is required for the realization of mixers for high signal frequencies. As has been discussed already in Chapter 5, Josephson junctions are such fast switches with switching times in the ps regime. Fig. 7.2b illustrates how a switch can be realized using the nonlinear quasiparticle IVC of a superconducting tunnel junction. During one half-period of the local oscillator signal the switch is open ($R = R_{\mathrm{sg}} \rightarrow \infty$), whereas during the other half-period of the LO signal the switch is closed ($R = R_N$). The resulting mixing device is the SIS mixer discussed below.

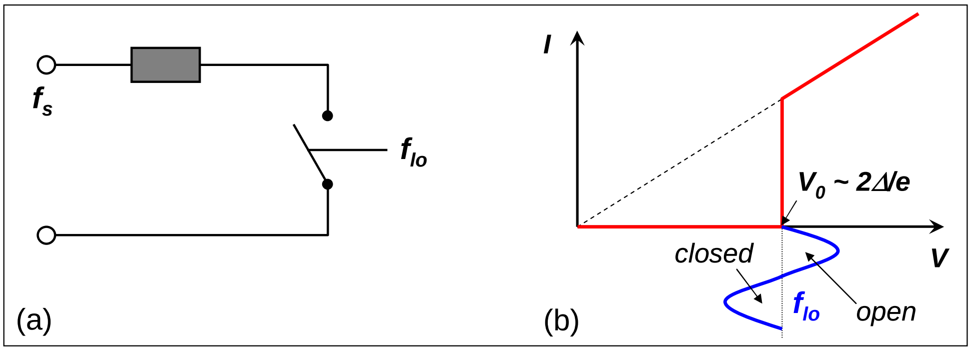

Figure 7.2: (a) Realization of an ideal mixer by a switch that is opened and closed at frequency f_{lo}. (b) Realization of the switch by the nonlinear IVC of a superconducting SIS junction.

More mathematically, a mixer is a nonlinear circuit or device that accepts as its input two different frequencies and presents at its output (i) a signal equal in frequency to the sum of the frequencies of the input signals, (ii) a signal equal in frequency to the difference between the frequencies of the input signals, and, if they are not filtered out, (iii) the original input frequencies. If the two frequencies that are to be mixed are e.g. sinusoidal voltage waves, they can be represented as:

$$\begin{aligned} v_s(t) &= a_s \cos(2\pi f_s t) = a_s \cos(\omega_s t) && (7.1.5) \\ v_{\mathrm{lo}}(t) &= a_{\mathrm{lo}} \cos(2\pi f_{\mathrm{lo}} t) = a_{\mathrm{lo}} \cos(\omega_{\mathrm{lo}} t) \quad , && (7.1.6) \end{aligned}$$

where v_s and v_{lo} represent the two varying voltages, a_s and a_{lo} the respective voltage amplitudes, and f_s and f_{lo} their frequencies (e.g. the signal and the LO frequency), respectively. If we can find a way to multiply these two signals by each other at each instant in time, we could apply the trigonometric identity

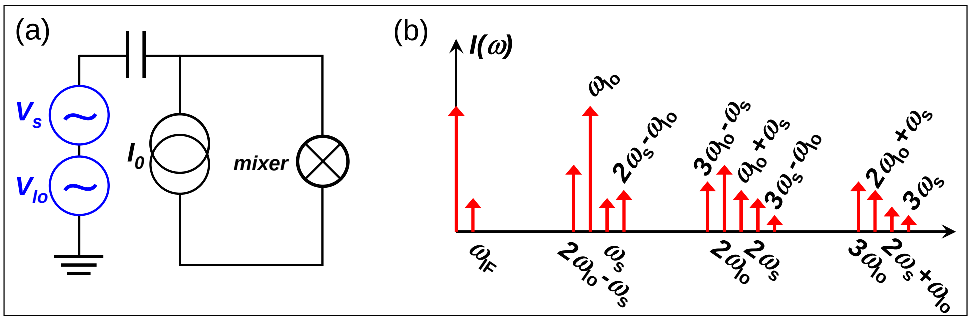
(a)
V_s
V_{lo}
I_0
mixer
(b)
$I(\omega)$
ω_{lo}
$2\omega_s$-ω_{lo}
$3\omega_{lo}$-ω_s
ω_{lo}+ω_s
$3\omega_s$-ω_{lo}
$2\omega_{lo}$+ω_s
$3\omega_s$
ω_{IF}
$2\omega_{lo}$-ω_s
ω_s
$2\omega_{lo}$
$2\omega_s$
$3\omega_{lo}$
$2\omega_s$+ω_{lo}

Figure 7.3: (a) Schematic circuit diagram and (b) spectrum of current response of a heterodyne mixer. Usually only the IF frequency $\omega_{\rm IF} = \omega_s - \omega_{\rm lo}$ is amplified and the other components are filtered out.

$\cos(A) \cdot \cos(B) \equiv \frac{1}{2}[\cos(A-B) + \cos(A+B)]$ and get

$$v_s(t) \cdot v_{\rm lo}(t) \quad = \quad \frac{a_s a_{\rm lo}}{2} \{\cos([\omega_s - \omega_{\rm lo}]t) + \cos([\omega_s + \omega_{\rm lo}]t)\} \quad . \tag{7.1.7}$$

That is, we obtain the sum $(\omega_s + \omega_{\rm lo})$ and difference $(\omega_s - \omega_{\rm lo})$ frequencies as required.

The next question is, how are we going to achieve this multiplication? In order to see this we assume that the mixer is a device with a nonlinear $I(V)$ dependence (IVC). For not too large voltage amplitudes we can express the current response by a power series (Taylor series)

$$I(t) \quad = \quad I_0 + \left.\frac{\partial I}{\partial V}\right|_{I=I_0} V + \frac{1}{2}\left.\frac{\partial^2 I}{\partial V^2}\right|_{I=I_0} V^2 + \frac{1}{6}\left.\frac{\partial^3 I}{\partial V^3}\right|_{I=I_0} V^3 + \ldots \quad . \tag{7.1.8}$$

If $V(t) = a_s \cos\omega_s t$, the linear term is proportional to $\cos\omega_s t$ and the quadratic proportional to $\cos^2\omega_s t = \frac{1}{2}[1 - \cos 2\omega_s t]$. That is, the quadratic term yields a static contribution to I as well as a contribution at $2\omega_s$. The cubic term yields contributions at ω_s and $3\omega_s$ etc.. We see that the nonlinear terms yield higher harmonics of the incoming signal.

If we now use as input signal the sum of two voltage signals at frequencies ω_s and $\omega_{\rm lo}$, the quadratic term results in a contribution of the form $\cos\omega_s t \cos\omega_{\rm lo} t$ given by (7.1.7). For $\omega_s \simeq \omega_{\rm lo}$ we obtain $\omega_{\rm IF} = |\omega_s - \omega_{\rm lo}| \ll \omega_s$ and we say that the signal is downconverted to the intermediate frequency. In the same way, the higher order terms in (7.1.8) yields frequency components at $|2\omega_s - \omega_{\rm lo}|$, $|2\omega_{\rm lo} - \omega_s|$, $|3\omega_{\rm lo} - \omega_s|$, etc.. We also see that the prefactor of the of the contribution resulting from the quadratic term is proportional to the second derivative of the IVC. Therefore, the nonlinearity of the IVC should be large in order to give a large value of $\frac{\partial^2 I}{\partial V^2}$. Fig. 7.3 shows the schematic circuit of a heterodyne mixer and the spectrum a current responses.

Single and Double Side Band Detection

The basic goal of a mixer is to effectively convert the signal at frequency $f_s = \omega_s/2\pi$ down to the intermediate frequency $f_{\rm IF}$ without adding much noise. In this process both the signal frequency $f_s = f_{\rm lo} + f_{\rm IF}$ and its mirror frequency $f_s = f_{\rm lo} - f_{\rm IF}$ can contribute. Depending on whether both frequencies are accepted or whether one of them is filtered out we distinguish between ***Double Side Band (DSB)*** or ***Single Side Band (SSB)*** receivers.

For most heterodyne receivers response is obtained from both sidebands $\omega_s = \omega_{\rm lo} \pm \omega_{\rm IF}$. Therefore, care must be taken in obtaining the noise temperature of SSB receivers from the measured DSB. When $\omega_{\rm IF} \ll \omega_s$, the receiver response is fairly flat in frequency so that $T_N({\rm SSB}) \simeq 2T_N({\rm DSB})$.

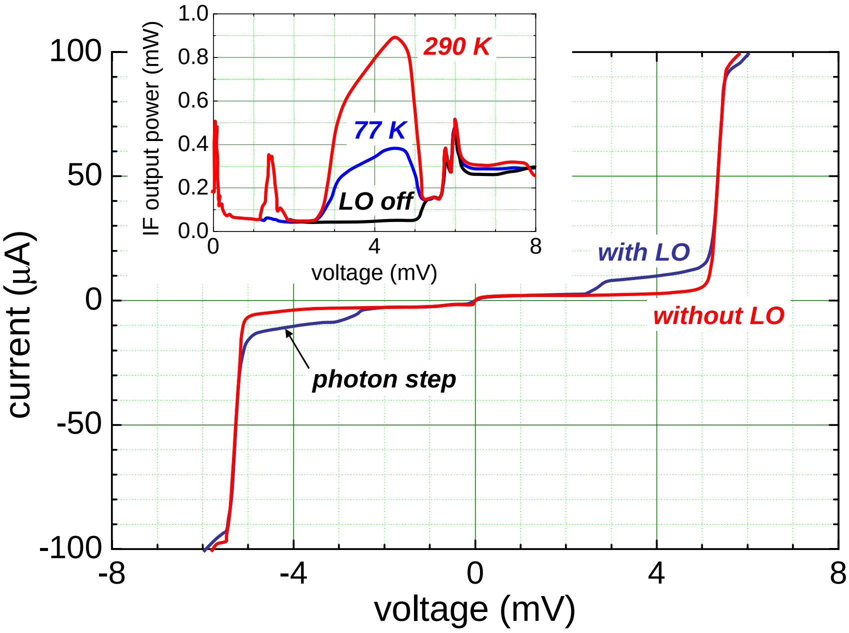

Figure 7.4: IVCs of an Nb/AlO$_x$/Nb SIS mixer (two junctions in series) with the LO switched on and off. The photon step corresponding to the LO frequency of 332 GHz is clearly seen. The curves in the lower-right-hand corner show the IF output power versus the bias voltage (according to H. Rothermel *et al.*, J. Physique IV **C6**, 267 (1994)).

Conversion Loss

An important quantity of a mixer is the ***conversion loss***

$$L_M = \frac{P_s}{P_{\rm IF}} = \frac{\text{signal power available at input}}{\text{IF power coupled to IF amplifier}} \quad . \qquad (7.1.9)$$

Generally, mixers have a conversion loss, i.e. $L_M > 1$ for DSB and $L_M > 2$ for SSB. However, some mixers also can produce conversion gain so that $L_M(\text{DSB}) < 1$ and $L_M(\text{SSB}) < 2$. The signal conversion is the larger the more nonlinear the mixer IVC. The ideal case would be a step-like change of the conductance as it is the case for an ideal switch shown in Fig. 7.2.

Figure 7.4 shows the IVCs of two series connected Nb junctions without and with LO power injection at 332 GHz. Note the low leakage current below and the sharp current onset at the gap voltage. Also shown are the IF output power curves for hot (290 K) and cold (77 K) loads, i.e. 290 and 77 K black body radiation. The receiver noise temperature determined for this receiver was 80 K.[6]

7.1.3 Noise Temperature of Heterodyne Receivers

Although there are various kinds of heterodyne receivers, they all fulfill the Dicke[7] radiometer equation.[8] If T_N is the noise temperature of the heterodyne receiver, according to the Dicke radiometer equation the temperature corresponding to the minimum detectable input signal is

---

[6] H. Rothermel, K.H. Gundlach, and M. Voß, J. Physique IV **C6**, 267 (1994).

[7] **Robert Henry Dicke**, born May 6, 1916, died March 4, 1997, was an American experimental physicist, who made important contributions to the fields of astrophysics, atomic physics, cosmology and gravity. Robert Dicke is also responsible for developing the lock-in amplifier, which is an indispensable tool in the area of applied science and engineering.

[8] J.D. Kraus, *Radio Astronomy*, 2nd edition, Powell, OH, Cygnus-Quasar (1986).

$$T_s^{\min} = \frac{T_N}{\sqrt{\Delta f \cdot \tau}} \quad . \tag{7.1.10}$$

Here, τ is the observation time in a frequency channel of bandwidth Δf. It is evident that by increasing the observation time we can reduce $T_s^{\min}$ by signal averaging. For a signal strength just corresponding to $T_s^{\min}$ we have SNR=1. Taking into account not only the noise of the receiver but also the contributions due to the atmosphere ($T_{\rm atm}$) and the antenna system ($T_{\rm ant}$) we can write the SNR as

$$\mathrm{SNR} = \frac{T_S \sqrt{\Delta f \cdot \tau}}{T_N + T_{\rm atm} + T_{\rm ant}} \quad . \tag{7.1.11}$$

For radiotelescopes, under good conditions $T_{\rm atm} + T_{\rm ant}$ is 40-50 K at about 100 GHz and an altitude of 2500 m. Hence, the receiver noise should be below about 30-50 K in order not to dominate the noise of the complete system. Whereas this is achieved for the 100 GHz regime, the situation is different at THz frequencies and high altitudes, where $T_{\rm atm} + T_{\rm ant} \ll T_N$.[9] Then according to (7.1.11) the observation time τ decreases proportional to T_N^2 on reducing the noise temperature of the receiver.

Referring to the block diagram shown in Fig. 7.1, the receiver noise temperature may be written as

$$T_N = T_{\rm in} + L_{\rm in} T_M + L_{\rm in} L_M T_{\rm IF} \quad . \tag{7.1.12}$$

Here, $T_{\rm in}$, T_M, and $T_{\rm IF}$ are the noise temperatures of the receiver input section, the mixer and the IF amplifier, respectively. The input section has the loss $L_{\rm in}$ and the mixer conversion loss $L_M = P_s/P_{\rm IF}$ is the ratio of the signal power P_s at the mixer input to the power $P_{\rm IF}$ coupled to the IF amplifier.

Eq.(7.1.12) reveals the sensitivity of the receiver noise to the mixer performance. The mixer should not only have a low noise temperature but also a low conversion loss. A mixer with conversion loss enhances, and a mixer with conversion gain reduces the IF amplifier noise contribution to the receiver noise temperature. Although for some mixers conversion gain is possible, practical receivers usually operate at $L_M(\mathrm{DSB}) \simeq 1$ and $L_M(\mathrm{SSB}) \simeq 2$, since conversion gain can lead to instabilities in the IF output. It has been shown by **Barber** that $T_M \approx 0$ can be achieved if the conductance waveform of a mixer consists of a series of narrow pulses, which can be realized by a switch with a small pulse-duty ratio $t/t_{\rm lo}$ where $t_{\rm lo} = f_{\rm lo}$.[10]

Before the development of superconducting SIS mixers, heterodyne receivers for radioastronomical and atmospheric observation were commonly based on Schottky diode mixers.[11,12] Typical receiver noise temperatures in the 690 and 830 GHz atmospheric window are above 2000 K DSB. Therefore, the reduction of the receiver noise to achieve shorter observation time, which is limited for example by weather conditions, was the motivation to look for other mixers. A further important limitation for Schottky mixers is the high LO power requirement for optimal mixing. This power usually ranges up to a few mW above 600 GHz, which is difficult to generate with sufficient frequency and amplitude stability.[13]

---

[9] In radioastronomy ground based observations are restricted to the so-called atmospheric frequency windows, where the atmospheric water vapor does not absorb the signals of interest. Therefore, especially in the lower THz range, astronomical measurements must be made from very high mountains, high flying aircrafts, balloons or from satellites. A project (ALMA, Atacama Large Millimetre Array) is under discussion to set up an array of 64 antennae at an altitude of 5000 m in Chile. The KAO (Kuiper Airborne Observatory), flying at an altitude of 14 km, was in use for many years. The successor will be SOFIA (Stratospheric Observatory For Infrared Astronomy), for which a telescope with the receivers will be mounted in a modified Boeing 747. Another project is the satellite FIRST (Far InfraRed and Submillimeter Space Telescope). The latter two projects aim for frequencies up to 2.5 THz.

[10] M.R. Barber, IEEE Trans. Microwave Theory Techniques **15**, 629 (1967).

[11] J. Zmuidzinas, A. Betz, and D.M. Goldhaber, Astrophys. J. **L75**, 307 (1986).

[12] A.I. Harris, D.T. Jaffe, J. Stutzki, and R. Genzel, Int. J. Infrared Millimeter Waves **8**, 857 (1987).

[13] K.F. Schuster, A.I. Harris, and K.H. Gundlach, Int. J. Infrared Millimeter Waves **14**, 1867 (1993).

7.1.4 SIS Quasiparticle Mixers

The desired switching type behavior required for an ideal mixer can be obtained with the quasiparticle tunneling IVC of an SIS junction shown schematically in Fig. 7.2b, because for $T \to 0$ the subgap conductance should go to zero. Biasing the junction just below the gap voltage $V_g = 2\Delta/e$, already a small local oscillator signal is sufficient to periodically switch the junction between the high- and low-conductance state. Note that the Josephson current has to be suppressed to zero by applying a magnetic field parallel to the junction.

It was, however, soon realized that this classical picture for frequency mixing is too simple because SIS junctions exhibit photon-assisted tunneling when exposed to radio frequency (RF) irradiation. As discussed in section 3.3.4, the absorption/emission of n local oscillator photons by a quasiparticle provides/costs the energy $n\hbar\omega_{\rm lo}$ thereby opening an additional photon assisted path for tunneling at the bias voltages

$$V_n = \frac{2\Delta \pm n\hbar\omega_{\rm lo}}{e} \quad . \tag{7.1.13}$$

This quantum effect leads to steps of the width $\hbar\omega_{\rm lo}/e$ in the IVC (cf. Fig. 3.15 or 7.4).

The quantum theory of quasiparticle SIS mixers was developed by **Tucker**[14,15] and thereafter analyzed in detail by **Richards** *et al.*,[16] **Shen** *et al.*,[17] **Hartfuß** and **Tutter**,[18] **Tucker** and **Feldman**,[19] **Winkler**[20] and others. Although the quantum theory of SIS mixers is quite complicated, the essential results can be summarized as:

1. the mixer can have conversion gain.
2. the mixer noise temperature can reach the quantum limit $T_N^{\rm q} = \hbar\omega/2k_B$.[21]
3. the optimum local oscillator power is relatively small. If the mixer operates in the middle of the first photon step below the gap voltage, the optimum local oscillator power is[22]

   $$P_{\rm lo}^{\rm opt} = \frac{2(\hbar\omega_{\rm lo})^2}{e^2 R_N} \quad . \tag{7.1.14}$$

   With a junction normal resistance $R_N = 50\,\Omega$ this gives $P_{\rm lo}^{\rm opt} \simeq 0.4\,\mu$W at 750 GHz as compared to a few mW required for Schottky mixers at the same frequency.

Danchi and **Sutton**[23] found that quasiparticle SIS mixers can, in principle, be used up to twice the gap frequency $f_{2g} = 4\Delta/eh$. However, **Feldman**[24] predicted that the noise of an optimized receiver increases

---

[14] J.R. Tucker, *Quantum limited detection in tunnel junction mixers*, IEEE J. Quantum Electron **15**, 1234-1258 (1979).

[15] J.R. Tucker, Appl. Phys. Lett. **36**, 477 (1980).

[16] P.L. Richards, T.M. Shen, R.E. Harris, and F.L. Lloyd, *Quasiparticle heterodyne mixing in SIS tunnel junctions*, Appl. Phys. Lett. **34**, 345-347 (1979).

[17] T.M. Shen, P.L. Richards, R.E. Harris, and F.L. Lloyd, Appl. Phys. Lett. **36**, 777 (1980).

[18] H.J. Hartfuß and M. Tutter, Int. J. InfraRed Millimetre Waves **5**, 717 (1984).

[19] J.R. Tucker and M.J. Feldman, *Quantum detection at millimeter wavelength*, Rev. Mod. Phys. **57**, 1055 (1985).

[20] D. Winkler, PhD Thesis, University of Göteborg (1987).

[21] M.J. Feldman, IEEE Trans. Magn. **MAG-23**, 1054 (1987).

[22] K.H. Gundlach, *Principles of direct and heterodyne detection with SIS junctions*, in *Superconducting Electronics*, Nato ASI Series, Springer, Berlin (1989), p. 259-284.

[23] W.C. Danchi and E.C. Sutton, J. Appl. Phys. **60**, 3967 (1984).

[24] M.J. Feldman, Int. J. InfraRed Millimetre Waves **8**, 1287 (1987).

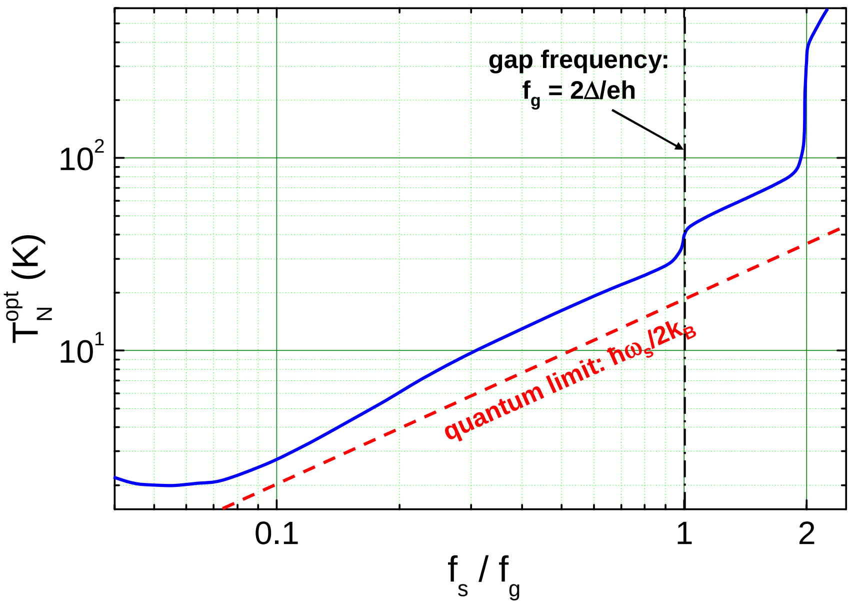

Figure 7.5: Calculated optimum noise temperature $T_N^{\rm opt}$ of a SIS quasiparticle mixer plotted versus the signal frequency f_s normalized to the gap frequency f_g. Also shown is the quantum limit for $f_g = 700$ GHz (Nb).

strongly when the signal frequency reaches $f_g = 2\Delta/eh$ but remains still reasonably low up to f_{2g}, above which the mixer performance drops very sharply. This result is summarized in Fig. 7.5. It is seen that over a wide frequency range the noise temperature of SIS quasiparticle mixers approaches the quantum limit. Practical devices do not reach the calculated optimum noise temperature. For example, mixers based on Nb junctions and an integrated Al matching circuit reach noise temperatures ranging between 680 and 1 700 K at frequencies ranging between 800 GHz and 1 THz.[25] A summary of experimentally determined noise temperatures is given in Fig. 7.6.

Frequency Limitations

As shown by Fig. 7.5 the energy gap of the superconducting material sets fundamental frequency limits for the mixing process and, moreover, for the surface resistance of the embedding circuit, which usually also contains a planar antenna. The gap frequency is about 700 GHz for Nb, 1.2 THz for NbN and several THz for high temperature superconductors.

Whereas Nb junctions with Nb embedding circuits are the first choice for frequencies below about 700 GHz, since Nb technology is well understood and presently provides lowest receiver noise temperatures, for frequencies above about 700 GHz Nb should be replaced by NbN. However, so far it is difficult to fabricate good tunnel junctions for this materials. Reasonable results have been obtained with NbTiN/MgO/NbTiN or Nb/Al-AlN$_x$/NbTiN structures.[26,27,28] These junctions could be used up to about 1 THz. An alternative material is the recently discovered superconductor MgB$_2$. However, it is not known whether tunnel junctions of sufficient quality can be made from this material. The high temperature superconductors are not used for SIS mixer. Due to the $d_{x^2-y^2}$ symmetry of the order parameter, for

---

[25] for a recent review see K.H. Gundlach, *SIS and bolometer mixers for terahertz frequencies*, Supercond. Sci. Techn. **13**, R171-R187 (2000).

[26] M. Schicke, PhD Thesis, University of Hamburg, Germany (1998).

[27] J.W. Kooi, J.A. Stern, G. Chattopadhyay, H.G. LeDuc, B. Bumble, and J. Zmuidzinas, Proc. 9th Int. Symp. on Space Terahertz Technol. , Pasadena, CA (1998), p. 283.

[28] B. Bumble, H.G. Leduc, and J.A. Stern, Proc. 9th Int. Symp. on Space Terahertz Technol., Pasadena, CA (1998), p. 295.

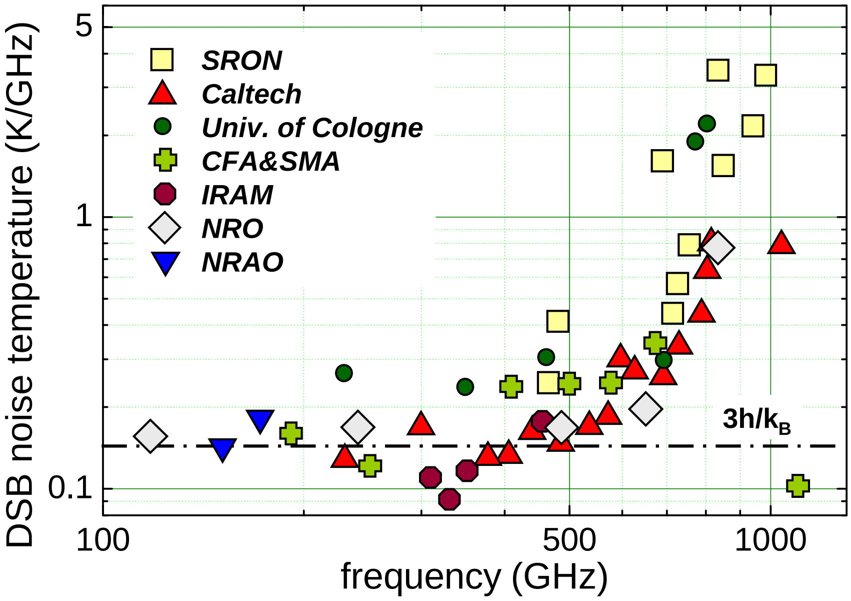

Figure 7.6: Measured DSB noise temperature of Nb based SIS quasiparticle mixers developed at different laboratories. The receiver noise temperatures fall in the range of $3-5\hbar\omega_s/k_B$ in the frequency range between 100 and about 600 GHz.

these junctions no sharp quasiparticle IVCs with negligible subgap conductance and a sharp increase of conductance at the gap voltage can be obtained.

A further frequency limitation is related to the junction capacitance. The geometrical capacitance of the SIS junction tends to short circuit the high frequency signal. The junctions are therefore usually embedded in a tuning circuit, which compensates for the SIS capacitance C and performs impedance transformation if required. Nevertheless, the large specific capacitance increasingly poses problems with increasing signal frequency.

The parallel-plate capacitor formed by the SIS junction is treated as an element of the embedding RF circuit. For its capacitance one has to find a compromise. To short circuit higher harmonics in the mixing process C should be sufficiently large. However, if C is too large it cannot be tuned out over the desired signal frequency bandwidth. Empirically, one came to the conclusion that optimized receivers must be designed with

$$\omega_s R_N C \quad \simeq \quad 2-4 \quad . \tag{7.1.15}$$

Inserting $R_N \simeq 4/\omega_s C$ into the BCS expression $J_c \simeq \frac{\pi}{4}\frac{2\Delta}{e}\frac{1}{R_N A}$ for the critical current density, we arrive at the expression

$$J_c \quad \simeq \quad \frac{\pi}{16}\frac{2\Delta}{e}\frac{C}{A}\omega_s \quad . \tag{7.1.16}$$

The specific capacitance $C_s = C/A = \epsilon\epsilon_0 A/t$, where A is the junction area, ϵ the relative dielectric constant and t the thickness of the tunnel barrier, only varies proportional to $1/t$, whereas J_c depends exponentially on t. Therefore, in first order approximation C_s can be assumed constant and J_c has to increase linearly with increasing signal frequency. Furthermore, the normal resistance R_N is constrained to be in a narrow range around $50\,\Omega$ to ensure proper impedance matching at the mixer input and output. Then, keeping R_N constant the junction area A has to decrease as $1/\omega_s$. That is, going to higher frequencies smaller junctions with higher current densities are required. However, this goal is difficult

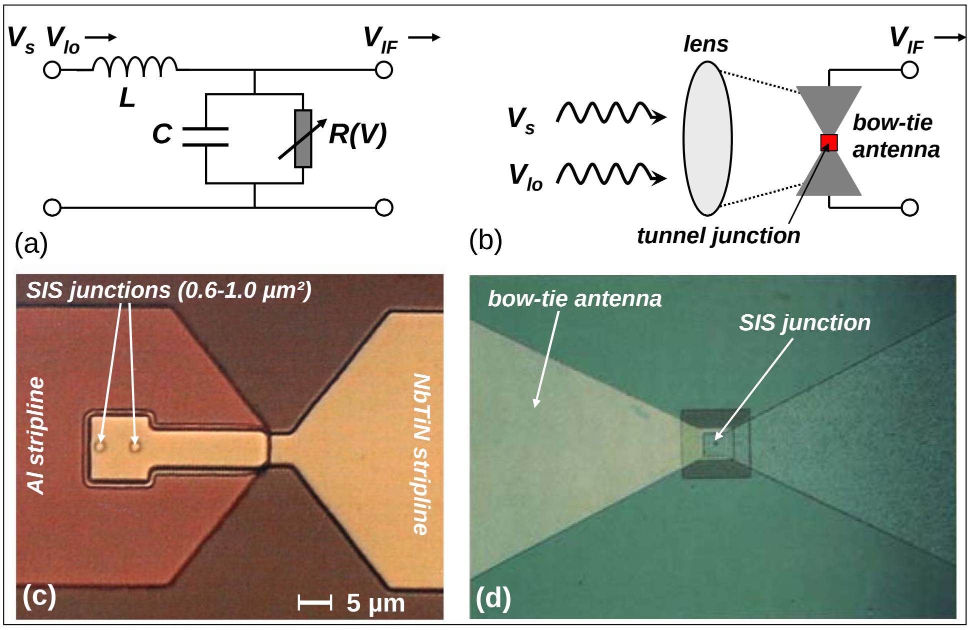

Figure 7.7: High frequency coupling schemes for SIS mixers. (a) A waveguide is used to couple in the signal and the local oscillator. A transmission line is used to couple out the IF signal. (b) Quasi-optical coupling through a lens to a wide-band bow-tie antenna with the SIS tunnel junction located in the center. (c) and (d) Optical micrographs of two mixer chips showing the area around the junctions with a stripline structure (c) and a bow-tie antenna (d).

to achieve, because the junction quality usually decreases with increasing current density (e.g. larger subgap conductance due to pinholes in the very thin tunneling barrier). Furthermore, for lower junction quality the optimum noise temperature may be by almost an order of magnitude larger than the optimum noise temperature plotted in Fig. 7.5. For example, for Nb we have $I_cR_N \simeq \pi\Delta/2e \simeq 2\,\mathrm{mV}$, which gives $I_c \simeq 40\,\mu\mathrm{A}$ for $R_N \simeq 50\,\Omega$. At $f_s = 500\,\mathrm{GHz}$ the condition $\omega_s\, R_N C \simeq 4$ results in $C \simeq 25\,\mathrm{fF}$. With the specific capacitance of Nb/AlO$_x$/Nb junctions of about $50\,\mathrm{fF}/\mu\mathrm{m}^2$, the required junction area is about $A \simeq 0.5\,\mu\mathrm{m}^2$ and, in turn, the required current density is as high as $J_c \simeq 8\,000\,\mathrm{A/cm}^2$.

High Frequency Design

An important aspect for the design of high frequency receivers is the coupling structure for the high frequency radiation. Since the junction size is much smaller than the free-space wavelength (3 mm at 100 GHz), a carefully designed waveguide and antenna structure is required (see Fig. 7.7). Waveguides are intrinsically relatively narrow band and become more difficult to work with as the wavelength moves into the submillimeter regime. In this regime, a thin film antenna structure is preferable including bow-tie and spiral antennas.[29] These antennae can be fabricated lithographically using the same material as for the junctions or using a material with a larger energy gap to reduce the surface resistance. The radiation may be focused on the antenna quasi-optically using a lens made out of an appropriate material (e.g. quartz or Teflon).

---

[29] M.J. Wengeler, *Submillimeter wave detection with superconducting tunnel diodes*, Proc. IEEE **80**, 1810 (1992).

7.1.5 Josephson Mixers

A mixer also can be realized by using the nonlinear IVC of a strongly overdamped Josephson junction. At this point we make a few remarks on the Josephson mixer.[30] The Josephson mixer can also have conversion gain[31] and needs little local oscillator power. Experimental and theoretical results indicate that the best noise temperature of Josephson mixers is of the order of 40 times the larger of either the physical temperature or the quantum limit $hf_s/2k_B$.[32,33] The noise is partly related to the fact that the Josephson junction is a nonlinear oscillator, which downconverts many high frequency noise components. Despite a variety of experiments, and some results which surpassed the above mentioned noise figures, up to now experimental Josephson mixers are not competitive with the quasiparticle mixers, if lowest noise temperatures are required. Note that in the quasiparticle mixer the Josephson currents and effects related to it, such as the return voltage V_r (cf. section 3.3) and Shapiro steps, can conflict with the optimal operation of the quasiparticle mixer. To avoid or reduce these effects pair tunneling is suppressed by an external magnetic field.

Of course, the high temperature superconductors can be used for the fabrication of Josephson mixers. However, the noise temperature of the best high-T_c Josephson mixers is also still considerably higher than that of corresponding low-T_c SIS mixers (Harnack et al 1998). Nevertheless, high-T_c Josephson mixers can be of interest for the THz frequency range because their upper frequency limit is set by the Josephson characteristic frequency $\omega_c = 2eI_cR_N/\hbar$ with $I_cR_N \simeq \pi\Delta/2e$ and therefore is about a factor of 10 above the low-T_c mixers. Recently, the Josephson mixer theory has been re-examined and it was found that under appropriate conditions (e.g. device parameters $I_cR_N \simeq 10\,\mathrm{mV}$, $R_N \simeq 50\,\Omega$) the noise temperature can be as low as about five times the physical temperature T for $\hbar\omega_{\mathrm{lo}} < k_BT$ and 10 times the quantum noise for $\hbar\omega_{\mathrm{lo}} > k_BT$. These promising new predictions have not yet been confirmed by experiments.

---

[30] P.L. Richards, *The Josephson junction as a detector of microwave and far-infrared radiation*, in *Semiconductors and Semimetals*, R. C. Willardson and A. C. Beer eds., Vol. **12**, Academic, New York (1977), pp. 395-440.

[31] J. Taur, J. Claassen, and P.L. Richards, Appl. Phys. Lett. **24**, 101 (1974).

[32] J.R. Tucker and M.J. Feldman, *Quantum detection at millimeter wavelength*, Rev. Mod. Phys. **57**, 1055 (1985).

[33] J.H. Claasen and P.L. Richards, J. Appl. Phys. **49**, 4117 (1987).

7.2 Superconducting Microwave Detectors: Direct Detectors

A further modulation detector is the quasiparticle direct detector, which is also called square-law detector. This detector uses the nonlinearity of the quasiparticle tunneling IVC of SIS junctions to rectify an high-frequency signal.[34] In this case the incoming signal of power P_s is converted into a change ΔI of the dc current. Classically, the current to voltage conversion factor of such detector can be obtained form the Taylor's expansion (7.1.8) with the input signal $v_s(t) = a_s \cos(\omega_s t)$. We obtain

$$I(t) \;=\; I_0 + \left.\frac{\partial I}{\partial V}\right|_{I=I_0} a_s \cos(\omega_s t) + \frac{1}{2}\left.\frac{\partial^2 I}{\partial V^2}\right|_{I=I_0} [a_s \cos(\omega_s t)]^2 + \ldots \quad . \tag{7.2.1}$$

Neglecting higher order terms the current response ΔI is the time average of the third term on the right hand side (the time average of the second term vanishes), which is

$$\Delta I \;=\; \langle\overline{I(t)}\rangle - I_0 \;=\; \frac{1}{4}\left.\frac{\partial^2 I}{\partial V^2}\right|_{I=I_0} a_s^2 \quad . \tag{7.2.2}$$

The time average of the power absorbed by the junction is

$$\alpha P_s \;=\; \frac{a_s^2}{2R_\mathrm{d}} \;=\; \frac{1}{2}\left.\frac{\partial I}{\partial V}\right|_{I=I_0} a_s^2 \quad . \tag{7.2.3}$$

Here, $\alpha \leq 1$ is a constant and R_d is the differential resistance at $I = I_0$. With (7.2.3) and (7.2.2) we obtain the current-to-power conversion factor $\eta_c = \Delta I / P_s$ of the junction to

$$\boxed{\eta_\mathrm{c} \;=\; \frac{\alpha}{2}\,\frac{\left.\frac{\partial^2 I}{\partial V^2}\right|_{I=I_0}}{\left.\frac{\partial I}{\partial V}\right|_{I=I_0}} \quad .} \tag{7.2.4}$$

This result obtained by a purely classical treatment is a good approximation as long as the onset of the quasiparticle current at the gap voltage is not too sharp. If not, a quantum mechanical treatment is required yielding[35,36]

$$\boxed{\eta_\mathrm{q} \;=\; \alpha\,\frac{e}{\hbar\omega_s}\,\frac{I(V_0+\hbar\omega_s/e) - 2I(V_0) + I(V_0-\hbar\omega_s/e)}{I(V_0+\hbar\omega_s/e) - I(V_0-\hbar\omega_s/e)} \quad .} \tag{7.2.5}$$

We see that the derivatives in the classical expression (7.2.4) are now replaced by the second difference of the unpumped IVC computed for the three points $V = V_0$ and $V = V_0 \pm \hbar\omega_s/e$, divided by the first difference computed between $V = V_0 \pm \hbar\omega_s/e$. If the current changes slowly on the voltage scale $\hbar\omega_s/e$, then the (classical) differential expression is a good approximation. For a tunnel junction with a sharp onset of the quasiparticle current we can use the approximations $I(V_0) = I(V_0 - \hbar\omega_s/e) \simeq 0$. Then with $\alpha = 1$ we obtain the quantum limit of the current-to-power response to

---

[34] H.J. Hartfuß and K.H. Gundlach, *Video detection of mm-waves via photon assisted tunneling between two superconductors*, Int. J. Infrared and Millimeter Waves **2**, 809 (1981).

[35] J. Tucker, *Quantum limited detection in tunnel junction mixers*, IEEE J. Quantum Electronics **15**, 1234-1258 (1979).

[36] J.R. Tucker and M.J. Feldman, *Quantum detection at millimeter wavelength*, Rev. Mod. Phys. **57**, 1055 (1985).

$$\boxed{\eta_{\rm q} \;=\; \frac{e}{\hbar\omega_s}\;.} \qquad (7.2.6)$$

This corresponds to about 2500 A/W at a frequency of 100 GHz in good agreement with experiments.[37]

We also could derive the quantum result by a qualitative discussion of the quantum nature of the detection process. To see this we note that for a purely classical detector the signal amplitude can be arbitrarily small resulting in a smooth change of the IVC due to the incoming signal. However, quantum effects become important, when the amplitude ea_s of the energy per electron is small and becomes comparable to the photon energy $\hbar\omega_s$. In the picture of photon assisted tunneling described in section 3.3.4, we obtain steps in the IVC at voltages $V_n = (2\Delta \pm n\hbar\omega_s)/e$. For large rf signals or small signal frequency ω_s, multi-photon events are likely and we obtain a series of voltage steps near the gap voltage which well approximate the rounded dc average obtained from classical theory. In contrast, for small signal amplitude and/or large photon energy only a single step is obtained since the multi-photon events are of higher order. Then, in the IVC only a single step would appear what is no longer in good agreement with the smooth classical IVC. That is, the classical result is a good approximation only for large signal amplitudes and/or small photon energy. Moreover, if the rise of the IVC at the gap voltage would be more gradual, also the series of discrete photon assisted steps would be smeared out making a classical treatment more appropriate. We finally note that that the discrete steps are not a particular feature of SIS tunnel junctions. The special feature is only their observability due to the sharpness of the gap structure in the IVC.

7.2.1 NEP of Direct Detectors

The sensitivity of the detector can be described by the noise equivalent power

$$\mathrm{NEP} \;=\; \sqrt{S_I(f)}\,\frac{P_s}{\Delta I} \;=\; \sqrt{\frac{\langle \Delta I^2\rangle}{B}}\;\frac{1}{\eta_{\rm q}}\;, \qquad (7.2.7)$$

where $S_I(f)$ is the current noise power spectral density in A^{2}Hz. At low temperature the Nyquist noise $S_I = 4k_BT/R$ usually can be neglected due to the small T and large R in the subgap regime of the SIS junction. The dominating noise source is shot noise $S_I(f) = 2eI$. With $S_I(f) = 2e(I_0 + I_s)$, where I_0 is the dark current and I_s the additional current due to the detected signal, we obtain

$$\mathrm{NEP} \;=\; \sqrt{2e(I_0+I_s)B}\;\frac{\hbar\omega_s}{e} \;=\; \sqrt{2(N_0+N_s)B}\;\hbar\omega_s\;. \qquad (7.2.8)$$

Here, $(N_0+N_s)B = (I_0+I_s)/e$ is the number of electrons flowing through the junction per time $\Delta t = 1/B$. For $I_0 \to 0$ the NEP approaches the value $\sqrt{2N_sB}\,\hbar\omega_s$. For example, for $N_sB = 1$/s we obtain NEP $\simeq 9\times 10^{-23}$W/$\sqrt{\text{Hz}}$ at $f_1 = \omega_1/2\pi = 100$ GHz. However, the experimentally measured values only range in the low 10^{-16}W/$\sqrt{\text{Hz}}$ regime for several 10 GHz.[38] That is, we require more than 10^{12} photons/s to achieve SNR=1. Evidently, we are far from single photon detection. The obvious reason is the fact that we cannot operate the detector at $I_0 \simeq 0$ but require a finite bias current that introduces shot noise.

---

[37] P.L. Richards, T.-M. Shen, R.E. Harris, F.L. Lloyd, *Superconductor-insulator-superconductor quasiparticle junctions as microwave photon detectors*, Appl. Phys. Lett. **36**, 480-482 (1980).

[38] Qing Hu and P.L. Richards, *Quasiparticle mixers and Detectors*, in *Superconducting Devices*, Steven T. Ruggiero and David A. Rudman (eds.), Academic Press Inc., San Diego (1990).

We also can estimate the optimum achievable NEP for SIS direct detectors. Doing so we point out that a specific advantage of SIS direct detectors is the fact that the current density in the subgap regime, i.e. the dark current, decreases exponentially with temperature due to the freeze out of thermally excited quasiparticles. For a dark current as small as 1 pA corresponding to about 10^7 electrons/s the sensitivity limit would be NEP $\simeq 3 \times 10^{-19}\mathrm{W}/\sqrt{\mathrm{Hz}}$ at 100 GHz. However, one has to take into account that the dark current of a SIS detector increases with the detector area A. In order to get orders of magnitude we consider a Nb based SIS junction with $I_cR_n \simeq 2\,\mathrm{mV}$. For $A = 100 \times 100\,\mu\mathrm{m}^2$ we obtain a normal resistance $R_n \simeq 2\,\Omega$ at a low current density $J_c \simeq 10\,\mathrm{A/cm}^2$. For a very high quality junction at low temperature the subgap resistance R_{sg} may be by a factor of about 1000 larger. Then, the dark current is $I_0 \simeq 2\,\mathrm{mV}/2000\,\Omega = 1\,\mu\mathrm{A}$. The corresponding shot noise limited sensitivity would be NEP $\simeq 2 \times 10^{-16}\mathrm{W}/\sqrt{\mathrm{Hz}}$ at 100 GHz.

7.3 Thermal Detectors

As the frequency of the incoming signal is increasing, we arrive at a situation where the detector can no longer follow the electromagnetic wave directly. Furthermore, in this regime, which is including the entire infrared regime, the signal due to individual photons is smaller than the noise floor making the detection of single photon events impossible. The detectors measure the average number of photons absorbed per unit of time, that is, the average power dissipated by the radiation. The simplest way to do this is with a thermometer, which determines the temperature rise δT in the detector due to the incoming radiation. Such detector is then denoted as ***thermal detector***. In some cases thermal equilibrium is not strictly reached in the detector and we have to deal with some effective temperature. In this case we usually speak about ***quasi-thermal detectors***. The most simple superconducting thermal detector is a superconducting transition edge bolometer, which uses the sharp change of the resistance of a superconducting film close to the critical temperature T_c. Thin film bolometers based on the metallic superconductors have been developed for sensitive infrared detection. With the discovery of the high temperature superconductors the superconducting bolometers have found renewed interest due to the relaxed cryogenic requirements for operation temperatures above 77 K.

7.3.1 Principle of Thermal Detection

The principle of thermal detection is sketched in Fig. 7.8. An incoming electromagnetic radiation of power P_s is absorbed by an absorber mass M, which has large absorptivity determined by its surface emissivity ε. The absorbed power heats up the complete sensor with the temperature rise determined by the heat capacity C of the sensor and P_s. Of course the sensor has to get rid again of the absorbed energy. This is happens by the following processes:

- radiation emission with the emitted power proportional to $\varepsilon A\sigma T^4$. Here, T is the detector temperature, A the area and $\sigma = 5.67 \times 10^{-8}\mathrm{W/m^2K^4}$ the Stefan-Boltzmann constant.
- direct thermal coupling to a heat sink of temperature T_S with the transferred heat being proportional to the thermal conductance G and the temperature difference $\delta T = T - T_S$.

If we take into account that the sensor is also heated up by the incident thermal radiation $P_b = bA\sigma T_b^4$ (b is a geometry dependent constant) from the background of temperature T_b, we can write down the heat balance equation as

$$\varepsilon(P_s + P_b) \quad = \quad C\,\frac{d(\delta T)}{dt} + G\,\delta T + a\varepsilon A\sigma T^4 \ . \tag{7.3.1}$$

Here, a is also a geometry dependent constant. Knowing the boundary conditions and the quantities C, G, and ε we can solve for δT, the quantity detected in an experiment, e.g. by the resistance change $\delta R = \frac{\partial R}{\partial T}\delta T$ of a superconducting film.[39]

For sufficient input power P_s we can usually neglect P_b and the radiative power emitted by the detector. However, one has to keep in mind that these powers introduce a certain amount of background noise. Assuming that the incoming power has a steady part P_0 and a time varying part $P_1 \mathrm{e}^{\imath\omega t}$ we obtain from (7.3.1)

$$\varepsilon(P_0 + P_s\mathrm{e}^{\imath\omega t}) \quad = \quad \imath\omega C\,\delta T\mathrm{e}^{\imath\omega t} + \widetilde{G}\delta T_0 + G\delta T\mathrm{e}^{\imath\omega t} \ . \tag{7.3.2}$$

---

[39] P.L. Richards, *Bolometers for infrared and millimeter waves*, J. Appl. Phys. **76**, 1-24 (1994).

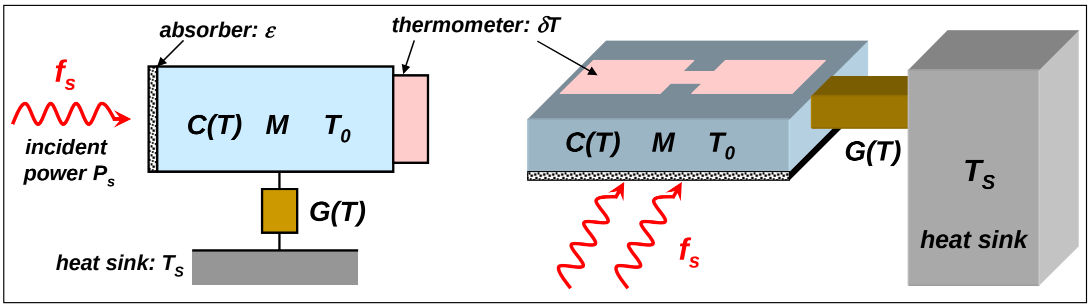

Figure 7.8: (a) Sketch of the general configuration of a thermal detector for electromagnetic radiation and (b) possible realization by weakly attaching a small mass to a heat sink.

Here, $\widetilde{G}$ is the heat conductance $\Delta P/\Delta T$ and G the dynamic heat conductance dP/dT. Equating the time independent terms gives the steady state heat flow equation that determines the average operation temperature T_0 of the bolometer

$$\delta T_0 = T_0 - T_S = \frac{\varepsilon P_0}{\widetilde{G}} . \tag{7.3.3}$$

Equating the time varying terms yields

$$\frac{\delta T}{P_s} = \frac{\varepsilon}{G + \imath\omega C} = \frac{\varepsilon}{G(1+\imath\omega\tau_{\rm th})} \tag{7.3.4}$$

with the thermal time constant $\tau_{\rm th} = C/G$.

Bolometers and Antenna-Coupled Microbolometer

Depending on whether the dissipative layer is larger or smaller than the wavelength of the incident radiation we can distinguish two different detector types. On the one hand, for infrared radiation the dissipative layer usually is much thicker than the wavelength. The radiation is absorbed completely by a layer of high absorptivity ε close to one. If the thermometer is a temperature-dependent resistance, we call this detector a ***bolometer***.

On the other hand, for far-infrared or sub-millimeter radiation, the dissipative layer is usually much thinner than the wavelength. The radiation power is collected via a dipole, bow-tie, logarithmic spiral or log-periodic antenna with efficiency η and the radiation induced electric power is dissipated in a few micrometer-sized thermal active element. This type of detector is called ***antenna-coupled microbolometer***.

Thermal Time Constants

In order to obtain a large detector response $\delta T/P_s$, the thermal conductance G, i.e. the coupling to the heat sink, should be small. However, a small G also results in a large thermal time constant $\tau_{\rm th} = C/G$. This immediately shows that in order to obtain a large sensitivity and a reasonably fast response one has to reduce C to a minimum. For example, this can be achieved by fabricating the detector element on a very thin substrate such as a membrane.

In order to give an example we estimate the thermal time constant of a YBCO microbolometer. For a 100 nm thick YBCO film with area 10 μm^2 we have a heat capacity of $C \simeq 10^{-11}$J/K at 90 K. If the

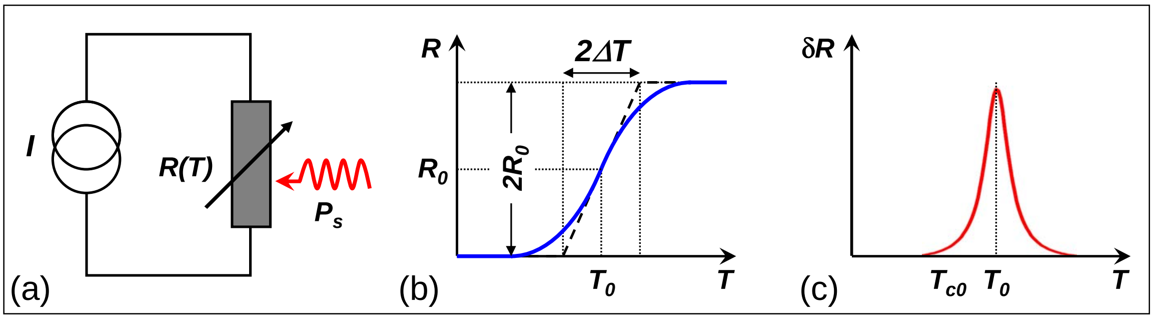

Figure 7.9: Operation principle of superconducting transition edge bolometer. (a) Circuit diagram of current biased superconducting strip. (b) Resistance vs. temperature curve (the dashed line shows the simplest approximation) and (c) typical response $\delta R(T)$.

thermal link is formed by four YBCO microbridges of length $10\,\mu$m and width $1\,\mu$m, we have $G \simeq 10^{-7}$W/K resulting in $\tau_{\rm th} \simeq 100\,\mu$s. This demonstrates that small bolometers can have fast response times. Note however, that in our simple estimate we have neglected substrate contributions. The situation in real thermal detectors is likely to be more complicated.

7.3.2 Bolometers

The operation principle of a superconducting transition edge bolometer is shown in Fig. 7.9. At T_0 the superconducting film has a resistance R_0 and a slope dR/dT. Usually, the temperature T_0 is chosen to have maximum slope dR/dT at T_0. Upon irradiation we obtain a temperature rise δT. However, the temperature rise also increases the resistance of the film. This results in an increase of the heat dissipation due to the external circuit (current source) equal to $I^2(R_0+\delta R) = I^2R_0 + I^2(dR/dT)\delta T e^{\imath\omega t}$. The heat balance equation for the time-varying terms gives then

$$\varepsilon P_s + I^2\delta R = C\,\frac{d(\delta T)}{dt} + G\,\delta T \qquad (7.3.5)$$

and further with $\delta R = (dR/dT)\delta T$

$$\varepsilon P_s = \delta T\left(G - I^2\,\frac{dR}{dT} + \imath\omega C\right) . \qquad (7.3.6)$$

With this expression we can obtain the ***responsivity*** S (in V/W) of the bolometer

$$\boxed{S = I\,\frac{\delta R}{P_s} = \frac{I}{P_s}\frac{dR}{dT}\,\delta T = \frac{dR}{dT}\,\frac{\varepsilon I}{G - I^2(dR/dT) + \imath\omega C} .} \qquad (7.3.7)$$

We see that we need a large dR/dT and small G and C to obtain a large responsivity . We can introduce the effective thermal conductance

$$G_{\rm eff} = G - I^2\,\frac{dR}{dT} = G - I^2R_0\beta , \qquad (7.3.8)$$

where

$$\beta = \frac{1}{R_0}\,\frac{dR}{dT} \simeq \frac{1}{\Delta T} \qquad (7.3.9)$$

is the temperature coefficient of the resistance R_0. For superconducting materials we have $\beta > 0$ and $G_{\rm eff} < G$ and we obtain

$$|S| = \frac{dR}{dT} \frac{\varepsilon I}{G_{\rm eff}(1+\omega^2\tau_{\rm eff}^2)^{1/2}} = \frac{\varepsilon I R_0 \beta}{G_{\rm eff}(1+\omega^2\tau_{\rm eff}^2)^{1/2}} \tag{7.3.10}$$

with the effective thermal time constant $\tau_{\rm eff} = C/G_{\rm eff}$. We see that we have to limit the bias current to

$$I^2 \lesssim K\,G\frac{dT}{dR} \quad \text{or} \quad I \lesssim \sqrt{\frac{K\,G\Delta T}{R_0}} \tag{7.3.11}$$

with typically $K \simeq 0.3-0.5$ in order to avoid a value $G_{\rm eff}$ too close to zero. For example, for $K = 0.3$ we have $G_{\rm eff} = 0.7G$ and $\tau_{\rm eff} = 1.43\tau$.

Noise Equivalent Power

In order to estimate the noise equivalent power (NEP) of bolometers we have to discuss the following noise contributions:

- ***Photon Noise:***

  The photon noise originates from the quasi-random emission of photons. Neglecting the fluctuations due to radiation emitted by the sensor, the NEP is determined by the total radiative power fluctuations. The square of the NEP is proportional to the detector area and the sum of the two terms due to contributions of the background (e.g. 300 K radiation through the detector field of view) and the cold shields. Both terms are proportional to T^5. The associated NEP is usually denoted as $\rm NEP_{BLIP}$ (BILP: Background Limited Infrared Photodetector).[40] A more detaile treatment of photon noise is given in Appendix D.

- ***Thermal Fluctuation Noise:***

  This noise results from thermodynamic energy fluctuations in the detector due to the random exchange of phonons (or electrons) through the thermal link which connects the detector to the heat sink at temperature T_0. It is usually referred to as phonon noise. The corresponding noise equivalent power is[41]

$$\mathrm{NEP_{th}} = \frac{\sqrt{4k_BT_0^2G}}{\varepsilon} . \tag{7.3.12}$$

---

[40] P.L. Richards, *Bolometers for infrared and millimeter waves*, J. Appl. Phys. **76**, 1-24 (1994).

[41] We use the thermal equilibrium mean square energy fluctuations $\langle \Delta u^2 \rangle = k_BT_0^2C$ in the system. In the bolometer there is a thermometer which reads out the fluctuation as $\Delta T = \Delta u/C$. The mean square temperature fluctuation can be written as an integral over the temperature spectral density $S_T(f)$ such that

$$\langle (\Delta T)^2 \rangle = \frac{k_BT_0^2}{C} = \int_0^\infty S_T(\omega)\frac{d\omega}{2\pi} .$$

We now use (7.3.4) (omitting for simplicity the thermal feedback due to the bias current) to relate the power fluctuations S_P to the temperature spectral density as $S_T = \varepsilon^2 S_P/(G^2+\omega^2C^2)$. From the above integral we obtain $S_P(\omega) = 2k_BT_0^2G/\pi\varepsilon^2$ or $S_P(f) = 4k_BT_0^2G/\varepsilon^2$.

- ***Nyquist Noise:***

  This noise is introduced by the voltage fluctuations with power spectral density $S_V = 4k_BT_0R_0$ (cf. section 3.1.4 and 3.5.5) in an ohmic resistor caused by the random motion of the charge carriers. In order to refer this voltage noise in the thermometer resistance to the detector input we can use the responsivity S. The corresponding noise equivalent power is

  $$\mathrm{NEP}_{\mathrm{Nyquist}} = \frac{\sqrt{4k_BT_0R_0}}{|S|} \; . \tag{7.3.13}$$

  For $G_{\mathrm{eff}} \sim G$ and $\tau_{\mathrm{eff}} \sim \tau$ we obtain

  $$\mathrm{NEP}_{\mathrm{Nyquist}} = \frac{G\Delta T}{\varepsilon I}\left(\frac{4k_BT_0}{R_0}(1+\omega^2\tau^2)\right)^{1/2} \tag{7.3.14}$$

  resulting in

  $$\frac{\mathrm{NEP}_{\mathrm{th}}}{\mathrm{NEP}_{\mathrm{Nyquist}}} = \frac{|S|^2T_0G}{\varepsilon^2R_0} \; . \tag{7.3.15}$$

  We see that thermal noise dominates for large $|S|$, T_0 and G. This is for example the case for bolometers based on the high temperature superconductors operating at $T_0 > 70\,\mathrm{K}$.

- $1/f$ ***Noise:***

  Low frequency $1/f$ noise originating from various sources (e.g. flux motion, trapping of charge carries in defects, etc.) causes fluctuations δR_f of the film resistance. The corresponding noise equivalent power is

  $$\mathrm{NEP}_{1/\mathrm{f}} = I\,\frac{\delta R_f}{|S|} = \frac{\delta R_f\Delta T}{\varepsilon R_0}\,G(1+\omega^2\tau^2)^{1/2} \; . \tag{7.3.16}$$

- ***Amplifier Noise:***

  Amplifier noise usually is small and can be neglected.

If all the different noise sources are uncorrelated, the total NEP is obtained to

$$\begin{aligned}\mathrm{NEP} &= \left(\mathrm{NEP}^2_{\mathrm{BLIP}} + \mathrm{NEP}^2_{\mathrm{th}} + \mathrm{NEP}^2_{\mathrm{Nyquist}} + \mathrm{NEP}^2_{1/\mathrm{f}}\right)^{1/2} \\ &= \left(\mathrm{NEP}^2_{\mathrm{BLIP}} + \widetilde{\mathrm{NEP}}\right)^{1/2} \; . \end{aligned} \tag{7.3.17}$$

For small enough bias current we can use $G_{\mathrm{eff}} \sim G$ and $\tau_{\mathrm{eff}} \sim \tau$ and obtain for the equivalent noise power contributed by the nonradiative effects as

$$\boxed{\widetilde{\mathrm{NEP}} = \frac{1}{\varepsilon}\left(4k_BT_0^2G + \frac{4k_BT_0}{I^2R_0}(G\Delta T)^2(1+\omega^2\tau^2) + \frac{\delta R_f^2}{R_0^2}(G\Delta T)^2(1+\omega^2\tau^2)\right)^{1/2} \; .} \tag{7.3.18}$$

This expression shows the important influence of the thermal conductance. In order to have high responsivity and low NEP, G should be as small as possible. However, this also increases the response time,

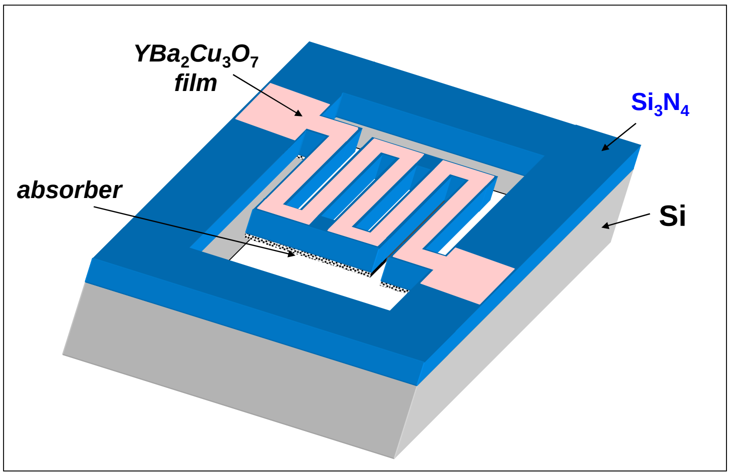

Figure 7.10: Sketch of a high temperature superconducting bolometer consisting of a meander shaped $YBa_2Cu_3O_{7-\delta}$ film deposited on a Si/Si_3N_4 substrate. Between the film and the Si_3N_4 usually a thin YSZ buffer layer is deposited. The SI substrate is removed below the bolometer area after the deposition process to achieve a free-standing structure with small heat capacity and small thermal coupling to the heat sink.

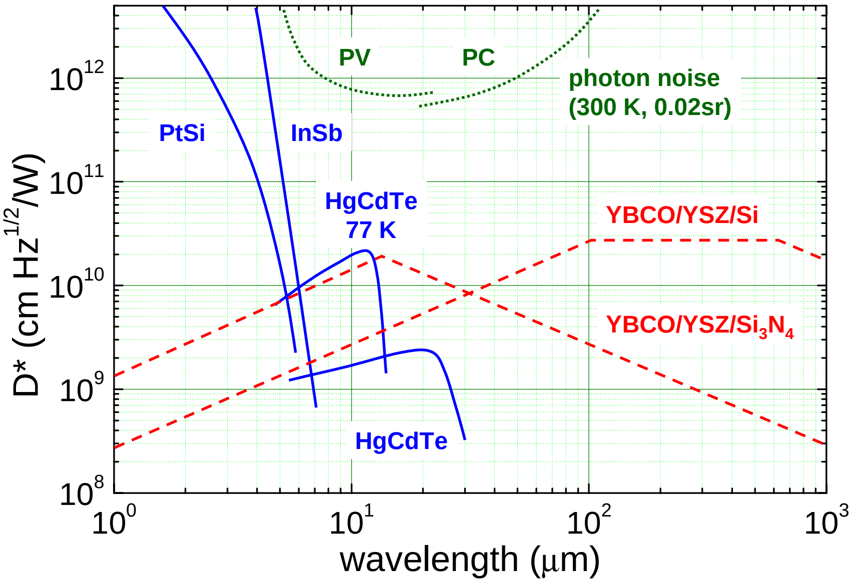

Figure 7.11: Specific detectivity $D^\star$ as a function of wavelength. The dashed lines show the predicted $D^\star$ for the high-T_c bolometers on silicon and Si_3N_4 membranes using YBCO thermometers. These lines were calculated using estimates for the minimum achievable heat capacity and thermal conductance and using measurements of the voltage noise of high-T_c thermometers. Typical values of $D^\star$ for InSb, PtSi, and HgCdTe detectors in two-dimensional staring arrays operated at 77 K are shown for comparison. Also shown are the photon noise limits for photovoltaic (PV) and photoconductive (PC) detectors, which view 300 K radiation in a 0.02 sr field of view (according to P.L. Richards, J. Appl. Phys. **76**, 1 (1994)).

which can be kept small by making C as small as possible. That is, both G and C should be as small as possible to achieve good detector performance.

In general, different detectors are compared with respect to their specific detectivity $D^\star = \sqrt{A}/\mathrm{NEP}$. Superconducting transition edge bolometer with $D^\star \simeq 10^{14}\mathrm{cm}\sqrt{\mathrm{Hz}}/\mathrm{W}$ at a wavelength of 500 μm and a temperature of 1.27 K have been fabricated using superconducting aluminium films on sapphire suspended by threads.[42] For microbolometers based on high temperature superconductors $D^\star \sim 10^{10}\mathrm{cm}\sqrt{\mathrm{Hz}}/\mathrm{W}$ and NEP $\sim 10^{-12}\mathrm{W}/\sqrt{\mathrm{Hz}}$ have been achieved at about 70-90 K. This detectivity is significantly better than $D^\star \sim 10^{8}\mathrm{cm}\sqrt{\mathrm{Hz}}/\mathrm{W}$ achieved for room temperature detectors. For instance, $\mathrm{YBa_2Cu_3O_{7-\delta}}$ meander-shaped films (see Fig. 7.10) have been deposited on micrometer thick $\mathrm{Si_3N_4}$ membranes with intermediate yttria-stabilized zirconia (YSZ) buffer layers.[43,44] Typical values obtained for various detectors are summarized in Fig. 7.11 including some cooled semiconductor detectors.[45]

Nonequilibrium Effects

So far we have assumed that the detector element always is in thermal equilibrium at an elevated temperature T. However, this is true only on sufficiently long time scales that allow for establishing thermal equilibrium. Fig. 7.12 illustrates the various interaction processes going on in a solid after the absorption of electromagnetic radiation. If the frequency of the incoming radiation is small, the energy usually is directly coupled to the electronic system and results in Joule heating of the electronic system. The heating only results in a change of energy distribution within a single band. If however the frequency is larger the absorption of a single photon can result in band to band transitions. The resulting high energy electronic excitations relax down to lower energies on a very short time scale τ_{ee} of the order of ps via electron-electron interactions. In this process a large number of low energy excitations is generated. This process again results in heating up the electronic system to an effective temperature $T_{\mathrm{eff}}^{\mathrm{el}}$. That is, after a very short time scale only the electronic system has established thermal equilibrium but there is no thermal equilibrium between electrons and phonons. Therefore, we can attribute an effective temperature $T_{\mathrm{eff}}^{\mathrm{el}}$ only to the electronic systems but not to the sample as a whole. The value of $T_{\mathrm{eff}}^{\mathrm{el}}$ is given by the radiation power and the heat capacity of the electronic system.

In a second step the electronic systems establishes equilibrium with the phonon system by electron-phonon interaction. This process occurs on a much longer time scale $\tau_{\mathrm{ep}} \sim 100\,\mathrm{ps}$. After this thermal equilibrium is established within the sample and we can can assign an effective temperature T_0 to the whole sample, which is of course above the temperature T_S of the heat sink. T_0 is determined by the total heat capacity of the sample. Finally, the excess heat is transferred to the heat sink of temperature T_S by thermal conduction. If the coupling to the heat sink is via an insulator, only the phonons contribute to this process and the characteristic time scale is given by the so-called phonon escape time τ_{es}. At low temperature this time depends on the temperature (roughly proportional to $1/T^3$) and the acoustic mismatch between the different materials. Typically, the phonon escape time is more than an order of magnitude larger than τ_{ep}. It becomes small for very thin films as discussed in section 7.3.3. Summarizing the discussion of the relaxation processes we can state that in most cases we have a three step process with $\tau_{\mathrm{ee}} \ll \tau_{\mathrm{ep}} \ll \tau_{\mathrm{es}}$. A simple description of the relaxation processes going on after the absorption of the incoming radiation can be given by rate equation.[46,47]

---

[42] J. Clarke, G.I. Hoffer, P.L. Richards, N.H. Yeh, *Superconductive bolometers for submillimeter wavelengths*, J. Appl. Phys. **48**, 4865-4879 (1977).

[43] S. Verghese, P.L. Richards, K. Char, D.K. Fork, T.H. Geballe, *Feasibility of infrared imaging arrays using high-T_c superconducting bolometers*, J. Appl. Phys. **71**, 2491-2498 (1992).

[44] S.J. Berkowitz, A.S. Hirahara, K. Char, E.N. Grossman, *Low noise high temperature superconducting bolometers for infrared imaging*, J. Appl. Phys. **69**, 2125-2127 (1996).

[45] P.L. Richards,*Bolometers for Infrared and Millimeter Waves*, J. Appl. Phys. **76**, 1 (1994).

[46] R. Gross, M. Koyanagi, *Effect of Electron Beam Irradiation on Superconducting Films* , J. Low Temp. Phys. **60**, 277 (1985).

[47] A.M. Kadin, A.M. Goldman, *Dynamical effects in nonequilibrium Superconductors*, in *Nonequilibrium Superconductivity*, D.N. Langenberg ed., North-Holland, Amsterdam (1986).

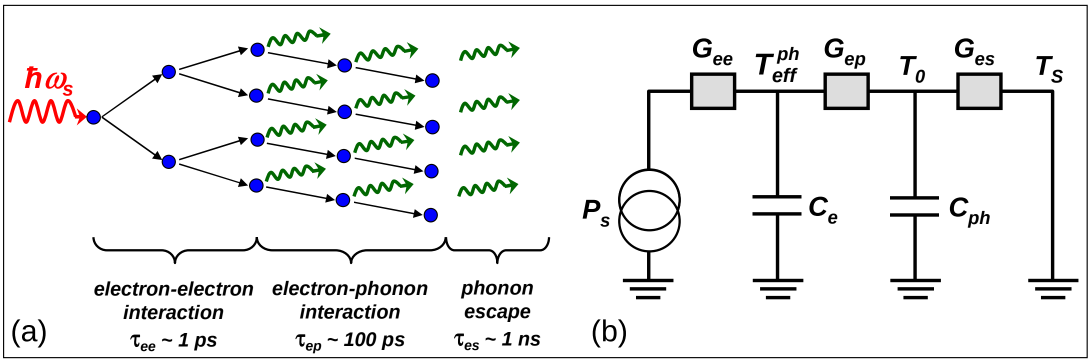

Figure 7.12: (a) Schematic illustration of the relaxation processes in a superconducting film deposited on a substrate after the absorption of electromagnetic radiation. (b) Equivalent circuit for the relaxation processes. The effective conductances are related to the relaxation times as $G_i = C_i/\tau_i$.

7.3.3 Antenna-Coupled Microbolometers

Antenna-coupled microbolometers are used for the thermal detection of far-infrared or millimeter radiation or the realization of so-called hot electron bolometers used for the direct detection and heterodyne detection of the same radiation. The typical configuration of an antenna-coupled microbolometer is shown in Fig. 7.13. The radiation is collected via an antenna structure (e.g. log-periodic or spiral antenna). Then the radiation induced electrical power is dissipated by a micrometer-sized thermometer such as a transition edge bolometer, a SIS junction, an inductance thermometer etc..

Transition-edge Microbolometers

For transition edge microbolometers the thermally active element is superconducting film positioned at the center of the antenna structure, which thermalizes the currents induced by the detected electromagnetic radiation. The impedance of the detector (about $80\,\Omega$) has to match the broadband antenna structure, which may be either normal or superconducting. A typical example is a high temperature superconducting microbolometer coupled to a log-periodic antenna as shown in Fig. 7.13. The thermally active element is for example an $YBa_2Cu_3O_{7-\delta}$ microbidge with width and length in the micrometer regime, which is suspended on a YSZ air-bridge. The free-standing YSZ structure is obtained by anisotropic chemical etching of the Si substrate. In this way a small thermal conductance between the bolometer and the substrate is established. At a temperature of about 85 K a responsivity of 1070 V/W was obtained for such structure and the estimated NEP was $3.2 \times 10^{-12}\mathrm{W}/\sqrt{\mathrm{Hz}}$.[48] Due to the small size and suspended structure both a small thermal conductance and small heat capacity could be realized resulting in a small thermal time constant of about $2\,\mu$s.

Hot Electron Microbolometers

A hot electron microbolometer consists of a superconducting antenna, a thin strip of normal metal acting as antenna load and a thermometer to measure the electron temperature in the piece of normal metal. Such structure is advantageous at very low operation temperatures and can act as sensitive detector for far-infrared and millimeter wave radiation.

At low operation temperatures the thermal insulation of the dissipative element (normal metal) as well as its temperature rise due to the detected radiation is enhanced due to the following reasons. Firstly, the

---

[48] M. Nahum, Qing Hu, P.L. Richards, S.A. Sachtjen, N. Newman, B.F. Cole, *Fabrication and measurement of high-T_c superconducting microbolometers*, IEEE Trans. Magn. **MAG-27**, 3081-3084 (1991).

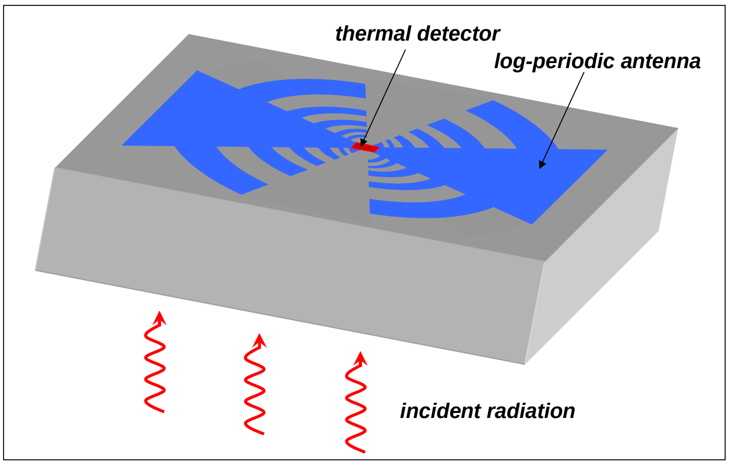

Figure 7.13: Schematic illustration of an antenna-coupled microbolometer. The thermal detector in the center of the antenna structure can be fabricated on a suspended structure (cf. Fig. 7.10) in order to realize a small heat capacity and thermal conductance and hence short thermal time constant.

thermal conductivity of insulators varies as T^3 and further the thermal conductance between the active element and the substrate varies roughly as T^3 (Kapitza thermal boundary resistance). This allows for a very efficient thermal decoupling of the absorber element from the environment going to low temperatures. Secondly, going to low temperatures the electron-phonon scattering time increases roughly as $1/T^3$ and reaches $\tau_{\mathrm{ep}} \gtrsim 10\,\mu$s at $T < 0.1$ K for copper.[49] Due to the large τ_{ep} the electron system effectively decouples form the lattice. That is, only a small amount of the detected radiation power is going into the lattice and mainly results in an increased electron temperature. Due to the decoupling between electron and phonons we can speak about hot electrons. Thirdly, if the active element is a normal conductor which is surrounded by superconducting material, the electronic excitations in the normal metal are trapped there due to Andreev reflection.[50] We see, that both the electrons and the phonons are trapped for a long time in the active detector area.

As a thermometer for the increased electron temperature $T_{\mathrm{eff}}^{\mathrm{el}}$ of the normal metal absorber a superconductor-insulator-normal metal (SIN) type junction is used. The normal electrode of this junction is just the absorber element. The electron temperature in the N layer can be measured via the quasiparticle tunneling current through the insulator. For such kind of microbolometer an extremely low NEP of a few $10^{-19}\mathrm{W}/\sqrt{\mathrm{Hz}}$ and a high responsivity of a few 10^9V/W is expected for an operation temperature of 0.1 K and a normal metal volume of about $1\,\mu\mathrm{m}^3$. The thermal conductance G between the electron and phonon systems is expected to be as low as about 10^{-13}W/K in this case. In experiments a responsivity of 10^9V/W was measured for $G = 2\times10^{-13}$W/K and a normal metal (copper) volume of about $1.5\,\mu\mathrm{m}^3$. The measured noise of $3\times10^{-18}\mathrm{W}/\sqrt{\mathrm{Hz}}$ was amplifier limited.[51]

Hot Electron Bolometer Mixer

The lack of SIS mixer technology for frequencies higher than about 1 THz (cf. section 7.1.4) initiated the search for alternatives. At present the most promising solution appears to be the ***hot electron bolometer (HEB) mixer*** shown in Fig. 7.14. It predominantly uses Nb or NbN microbridges as sensitive elements and offers the following advantages:

---

[49] M. Nahum, P.L. Richards, C.A. Mears, *Design analysis of novel hot electron microbolometers*, IEEE Trans. Appl. Supercond. **AS-3**, 2124-2127 (1993).

[50] An electron that wants to enter the superconducting material from the normal metal side cannot do so for energies smaller than the gap energy, since there are no available states in the superconductor below the gap energy.

[51] M. Nahum, J.M. Martinis, *Ultrasensitive hot electron microbolometers*, Appl. Phys. Lett. **63**, 3075-3077 (1993).

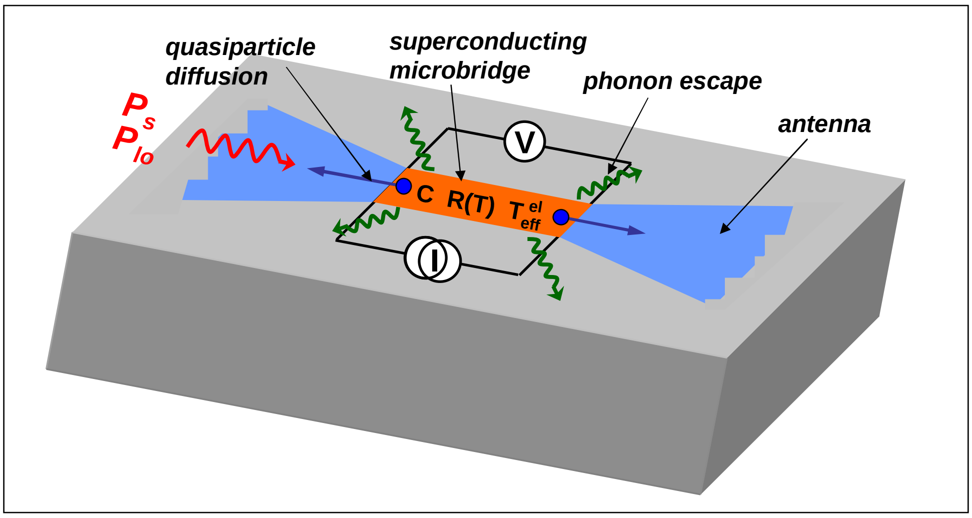

Figure 7.14: Schematic illustration of the hot electron bolometer mixer. The signal power P_s and the local oscillator power $P_{\rm lo}$ are detected by an antenna structure and transmitted through a superconducting microbridge operated as a transition edge bolometer. The heat is removed from the active area by phonon escape to the substrate and diffusion of hot electrons into the leads.

- the maximum signal frequency is not limited by the energy gap of the superconductor, enabling mixing up to several THz.
- the required local oscillator power is very low (about 20-1000 nW) and does not increase with frequency as for SIS mixers.
- for $f_s > 2\Delta(T)/h$ the rf impedance is expected to be essentially resistive and frequency independent. There are no harmonics of the LO and signal frequency because the thermal response of the bolometer is too slow. These two properties simplify the rf circuit design.
- a magnetic field to suppress Josephson currents is not required.

In contrast to diodes or SIS junctions with strongly nonlinear IVCs, the HEB is not switched by the local oscillator between high- and low-conductance states. The switching model mentioned in section 7.1.2 is therefore not appropriate for HEB mixers. The dissipated rf power coupled via the antenna into the microbridge can be written as

$$P(t) \;=\; \frac{1}{R}\left[v_{\rm lo}\cos(\omega_{\rm lo}t)+v_s\cos(\omega_s t)\right]^2 \;. \qquad (7.3.19)$$

Due to the finite thermal time constant, the bolometer is too slow to follow the power variation at $f_{\rm lo}$, f_s, and higher frequencies, but it should be fast enough to instantaneously respond to a power variation at the desired IF frequency $f_{\rm IF} = |f_{\rm lo} - f_s|$ of several GHz. We therefore obtain

$$P(t) \;=\; P_{\rm lo}+P_s+2\sqrt{P_{\rm lo}P_s}\,\cos(\omega_{\rm IF}t) \qquad (7.3.20)$$

with $P_{\rm lo} = v_{\rm lo}^2/2R$ and $P_s = v_s^2/2R$. The IF voltage amplitude can be written as

$$v_{\rm IF} \;=\; S\cdot 2\sqrt{P_{\rm lo}P_s} \;=\; \frac{dR}{dT}\,\frac{I}{G_{\rm eff}}\,\frac{2\sqrt{P_{\rm lo}P_s}}{(1+\omega_{\rm IF}^2\tau_{\rm eff}^2)^{1/2}} \qquad (7.3.21)$$

with the responsivity S given by (7.3.10).

For hf_S and $hf_{\rm lo} > 2\Delta$, the superconductor behaves nearly as a normal conductor and $R \simeq R_N$ in good approximation. Note that in the SIS mixer absorption of photons occurs by photon assisted tunneling. The absorber itself, the SIS junction, stays at the bath temperature. In contrast, in the HEB the absorption of photons results in a considerable increase in the electron temperature. Consequently, mixing is not limited by the energy gap and good performance is expected up to tens of THz. Equation (7.3.21) is misleading in the sense that an infinite increase of the LO power induces an infinite increase of the IF output voltage. This is in principle correct, but other effects not included in (7.3.21) limit the LO power level for bolometers. For the transition-edge bolometer the LO power must remain below the level at which it would heat the electron gas in the microbridge above T_c. Usually the temperature of the heat sink is chosen well below T_c and the LO power adjusted to a value that heats up the electron gas close to T_c.

A few conditions have to be satisfied to achieve the desired high intermediate frequency of several GHz. Firstly, only the electron gas but not the lattice should be heated. As discussed above, this can be achieved, if the electron-electron scattering time $\tau_{\rm ee}$ is much shorter than the electron-phonon scattering time $\tau_{\rm ep}$. Then the the electronic system reaches thermal equilibrium within a short time scale without the energy leaking into the phonon system. At low temperature, short $\tau_{\rm ee}$ between 10^{-10} and 10^{-12}s is obtained for very thin films in the dirty limit. Such films have large sheet resistance $R_{\rm sh} = \rho/d$, where ρ is the resistivity and d the film thickness. In good approximation we can express $\tau_{\rm ep}$ as[52,53]

$$\tau_{\rm ee} \quad \sim \quad \frac{10^{-8}\ [\rm s]}{R_{\rm sh}[\Omega/\Box]\ \ T_c[\rm K]} \tag{7.3.22}$$

For 10 nm thick Nb films sheet resistances between 12 and 28 $\Omega/\Box$ have been reported.[54,55] These films typically have $T_c \simeq 5$ K. For 10 nm thick NbN films, $R_{\rm sh} \simeq 70\,\Omega/\Box$ and $T_c \simeq 14$ K.[56] Fig. 7.15 shows optical micrographs of HEB mixers consisting of a NbN superconducting bridge with submicron dimensions contacted by thick gold pads.

The hot electrons can be cooled down by phonon emission, which escape into the substrate, and/or by the diffusion of hot electrons into normal metal contact pads. Depending on the dominating mechanism one speaks about ***phonon*** or ***diffusion cooling***.

Phonon Cooling: For phonon cooling we have an effective thermal time constant

$$\tau_{\rm eff} \quad = \quad \tau_{\rm ep} + \tau_{\rm es} \ll \tau_{\rm ee} \ . \tag{7.3.23}$$

For Nb the electron-phonon scattering time can be expressed as[57]

$$\tau_{\rm ep} \quad \sim \quad \frac{10^{-8}\ [\rm s]}{T_{\rm ph}^2\ [\rm K^2]}\ , \tag{7.3.24}$$

---

[52] P. Santhanam and D. Prober, Phys. Rev. **B 29**, 3733 (1984).

[53] E.M. Gershenzon, M.E. Gershenzon, G.N. Gol'tsman, A.M. Lyul'kin, A.D. Semenov, and A.V. Sergeev, Sov. Phys. Tech. **34**, 195 (1989); see also Sov. Phys. JETP **3**, 505 (1990).

[54] R.J. Schoelkopf, P.J. Burke, D.E. Prober, B. Karasik, A. Skalare, W.R. McGrath, M.C. Gaidis, B. Bumble, and H.G. LeDuc, IEEE Trans. Appl. Supercond. **AS-7**, 3576 (1997).

[55] M. Frommberger, M. Schicke, P. Sabon, K.H. Gundlach, and K.F. Schuster, Proc. 4th Eur. Conf. on Appl. Supercond. **Vol 2**, 667 (1999).

[56] S. Cherednichenko, P. Yagoubov, K. Il'in, G. Gol'tsman, and E. Gershenzon, Proc. 8th Int. Symp. on Space Terahertz Technol., Harvard University, Cambridge, MA (1997), p. 245.

[57] D.E. Prober, Appl. Phys. Lett. **62**, 2119 (1993).

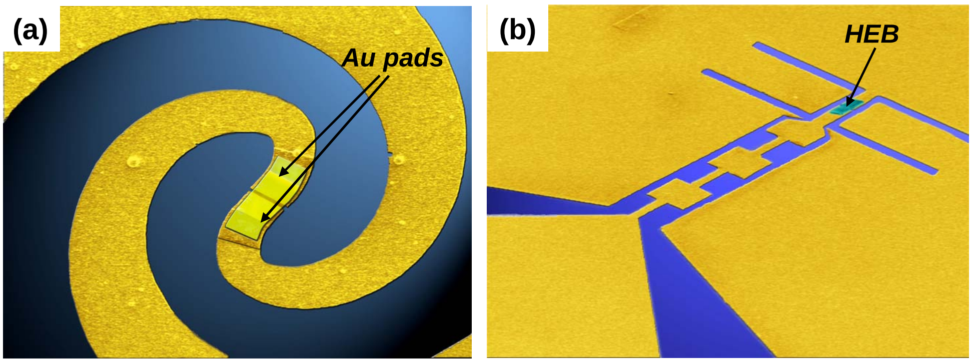

Figure 7.15: Optical micrographs of hot electron bolometer mixers consisting of a NbN superconducting bridge with submicron dimensions (not resolved in the micrograph) contacted by thick gold pads. (a) Spiral antenna and (b) twin slot antenna (micrographs curtesy of SRON, The Netherlands).

where $T_{\rm ph}$ is the phonon temperature. The escape time of phonons into the substrate can be written as[58]

$$\tau_{\rm es} \;\sim\; \frac{4d}{\gamma v_{\rm ph}} \;, \tag{7.3.25}$$

where d is the film thickness, $v_{\rm ph}$ the sound velocity in the bolometer material and γ the transmission coefficient of phonons at the bolometer/substrate interface, which includes acoustic mismatch.

To obtain effective phonon cooling the phonons generated in the microbridge by hot electrons should escape as fast as possible into the substrate and not feed back energy into the electron system. This requires $\tau_{\rm es} \ll \tau_{\rm ep}, \tau_B$. Here, τ_B is the pair breaking time of phonons with energy larger than 2Δ. These phonons can break up Cooper pairs and feed back their energy into the electron system. According to (7.3.25), $\tau_{\rm es} \ll \tau_{\rm ep}$ can be obtained by using very thin films. Then, $\tau_{\rm eff} \simeq \tau_{\rm ep}$, i.e. the electron-phonon scattering time determines the speed of the HEB, which in turn determines the IF bandwidth $1/2\pi\tau_{\rm ep}$ of the mixer. For Nb we have $\tau_{\rm ep} \simeq 1\,$ns giving $1/2\pi\tau_{\rm ep} \simeq 160\,$MHz. This is too narrow for radio astronomy applications. Better results are expected for NbN. Here, $\tau_{\rm ep} \simeq 15\,$ps for $d < 5\,$nm giving $1/2\pi\tau_{\rm ep} \simeq 10\,$GHz.

The SSB conversion gain $1/L_M = P_{\rm IF}/P_s$ has been calculated from (7.3.21). Assuming that the IF power is coupled into the matched load we obtain[59]

$$\frac{1}{L_M} \;=\; \left(\frac{dR}{dT}\,\frac{I}{G_{\rm eff}}\right)^2 \frac{P_{\rm lo}P_s}{2R_L}\,\frac{1}{1+\omega_{\rm IF}^2\tau_{\rm eff}^2} \;. \tag{7.3.26}$$

Here, R_L is the load resistance and $G_{\rm eff}$ is the electron-phonon thermal conductance, which is proportional to the volume V of the bolometer. We see that the conversion gain is increasing with increasing LO power and with larger dR/dT, i.e. with steeper $R(T)$ curves at the superconducting transition.[60]

The mixer noise is dominated by thermal fluctuations of the electron temperature. The contribution of the Nyquist noise is generally smaller and the contribution of the shot noise is negligibly small. The ultimate (SSB) mixer noise temperature, when the device is operated at temperatures $T \ll T_c$, can be expressed as[61]

---

[58] W.R. McGrath, J.A. Stern, H.H. Javadi, J.R. Cypher, B.D. Hunt, and H.G. LeDuc, IEEE Trans. Magn. **MAG-27**, 2650 (1995).

[59] W.R. McGrath, J.A. Stern, H.H. Javadi, J.R. Cypher, B.D. Hunt, and H.G. LeDuc, IEEE Trans. Magn. **MAG-27**, 2650 (1995).

[60] B.S. Karasik and A.I. Elant'ev, Proc. 6th Int. Symp. on Space Terahertz Technol., Pasadena, CA (1995), p. 229.

$$T_M \;=\; (n+2)\,T_c\;. \tag{7.3.27}$$

For phonon cooled NbN mixers $n \simeq 1.6$.

Diffusion Cooling: The idea of diffusion cooling is that the hot electrons escape from the absorber into the normal metal contact pads at the ends of the microbridge in a time shorter than the electron-phonon scattering time $\tau_{\rm ep}$.[62] To achieve this the length L of the bridge should be smaller than the diffusion length $\sqrt{D\tau_{\rm ep}}$ of the hot electrons within the time scale $\tau_{\rm ep}$. The diffusion constants of 10 nm thick superconducting films where found to range between 0.2 (NbN) and about 10 cm^2/s (Al). With $\tau_{\rm ep} \sim 10^{-10}$s this results in $L \lesssim 0.1\,\mu$m at $D = 1$ cm^2/s. The related IF bandwidth is $1/2\pi\tau_{\rm ep} = 1.6$ GHz. Note that the IF bandwidth increases as $1/L^2$, if the length of the microbridge is reduced further.

The theory of diffusion cooled HEB mixers is still a matter of controversy. Because it is a topic of ongoing actual research it will not be discussed in more detail here.

Superconducting Inductance Thermometers

Thermometers based on a resistive read-out have certain disadvantages. For example, biasing of the superconductor in the middle of the resistive transition is required. Furthermore, self-heating due to the bias currents limits the bias current range and in turn the available output voltage. Finally, nonzero resistance always gives rise to Nyquist noise limiting the sensitivity. Therefore, it would be advantageous to use a superconductor as a thermometer in the $R = 0$ state. This can be realized by superconducting inductance thermometers.

The inductance of superconducting circuit elements is given by the sum of the geometric inductance $L_{\rm geo}$ and the kinetic inductance $L_{\rm kin}$, which results from the inertia of the superconducting charge carriers. For a thin film element the total inductance per square can be expressed as

$$L_\square \;=\; L_{\rm geo} + L_{\rm kin} \;=\; \mu_0 \lambda_L \coth(d/\lambda_L)\;. \tag{7.3.28}$$

Here, d is the film thickness and λ_L the London penetration depth. The latter is strongly temperature dependent following

$$\lambda_L(t) \;=\; \frac{\lambda_L(0)}{\sqrt{1-t^4}}\;, \tag{7.3.29}$$

where $t = T/T_c$ is the reduced temperature. For thin films ($d/\lambda_L \lesssim 0.4$) the kinetic inductance is dominant. Approximating $\coth x \simeq 1/x$ we obtain

$$L_\square \;\simeq\; L_{\rm kin} \simeq \mu_0 \frac{\lambda_L^2}{d} \;=\; \mu_0\, \frac{\lambda_L^2(0)}{d(1-t^4)}\;. \tag{7.3.30}$$

Then

$$\frac{dL_\square}{L_\square dT} \;\simeq\; \frac{dL_{\rm kin}}{L_{\rm kin} dT} \simeq \frac{4t^3}{(1-t^4)T_c}\;. \tag{7.3.31}$$

---

[61] B.S. Karasik and W.R. McGrath, Proc. 9th Int. Symp. on Space Terahertz Technol., Pasadena, CA (1998), p. 73.

[62] D.E. Prober, Appl. Phys. Lett. **62**, 2119 (1993).

We see that $dL_\square/dT$ becomes larger when T approaches T_c, e.g. $\Delta L_\square/L_\square \simeq 18.5\Delta T/T_c$ at $t = 0.95$.

The strong temperature dependence of the kinetic inductance close to T_c results from the strong temperature dependence of the Cooper pair density in this temperature regime. It can be used for the realization of sensitive inductance thermometers. For the measurement of the inductance value sensitive SQUID sensors can be used. Although the kinetic inductance thermometers have not yet been fully optimized, a noise equivalent power of a few times 10^{-11}W/$\sqrt{\mathrm{Hz}}$ and a responsivity of a few times 10^6V/W have been achieved at $t = 0.8$ with a niobium device.[63]

---

[63] J.E. Sauvageau, D.G. McDonald, E.N. Grossman, *Superconducting kinetic inductance radiometer*, IEEE Trans. Magn. **MAG-27**, 2757-2760 (1991).

7.4 Superconducting Particle and Single Photon Detectors

With increasing quantum energy of the incoming radiation, the signal due to individual photons may become larger than the noise floor making the detection of single photon events possible. This is in contrast to the situation discussed in sections 7.2 and 7.3, where we have discussed the case that single photon events cannot be resolved and the detector only can measure the average number of photons absorbed per unit of time.

If for sufficiently large photon energy (e.g. in the visible, UV or x-ray regime) the signal generated by the absorption of a single photon exceeds the noise level, a measurable electrical signal is generated by the absorption of every single photon. Then, if the time interval between the incoming photons is larger than the characteristic time constant of the detector, one can use the detector to count the number of absorbed photons (photon counting mode). We also can average over the individual signal pulses to obtain the average rate of incoming photons (photon integrating mode). If we are able to resolve the dependence of the signal amplitude on the energy of the absorbed photon, we even can use the detector to determine the energy of each incoming photon. That is, we can use the detector as a radiation spectrometer. In this case for thermal detectors one usually refers to a ***microcalorimeter*** rather than a bolometer. Of course the various operation modes cannot only be applied to photon detection but also to the detection of particles such as electrons, protons, neutrons, α-particles, etc. which deposit their kinetic energy in the detector on absorption. Here, the particle absorption process also generates high energy excitations in the absorber material, which quickly relax down thereby heating up the electron and phonon systems in a similar way as during photon absorption.

At present two main types of high energy resolution superconducting photon/particle detectors exist. The first type, the ***superconducting tunnel junction detector (STJD)***, is a non-thermal detector. It extracts the charge carriers generated by the photon/particle absorption before they thermalize with the lattice. The other type, the ***microcalorimeter***, is a thermal detector. It measures a temperature variation generated by the photon/particle absorption. Both detector types are briefly addressed in the following subsections. Until today, superconducting particle/photon detector and spectrometers have been developed into a powerful technology. In particular, cryogenic spectrometers are beginning to enable new types of measurements. Spectrometers based on superconducting tunnel junctions (STJ) and transition edge sensors (TES) already have been used in various applications such as high sensitivity astronomical imaging in the optical to soft x-ray regime or x-ray microanalysis of biological and industrial materials.[64,65,66,67,68,69]

7.4.1 Thermal Photon and Particle Detectors: Microcalorimeters

The operation principle of a thermal single photon/particle detector is the same as that described in section 7.3. The absorption of a single photon or particle heats up the sensor volume and the temperature rise is measured by a sensitive thermometer. If a transition-edge bolometer is used as thermometer the detectors are referred to as ***transition edge sensors (TES)***. We note that in contrast to the antenna-coupled microbolometers we do not need a collecting antenna structure, because the wavelength of the detected photons (visible to x-ray regime) and particles is smaller than the detector size. The incoming photon/particle is rather absorbed directly in the sensor volume, which may be covered by a layer of high

---

[64] D. Twerenbold, *Cryogenic particle detectors*, Rep. Prog. Phys. **59**, 349-426 (1996).

[65] K. D. Irwin, G. C. Hilton, D. A. Wollman, and J. M. Martinis, Appl. Phys. Lett. **69**, 1945 (1996).

[66] F. Scott Porter, Nucl. Instrum. Methods Phys. Res. **A 520**, 354 (2004).

[67] D. A. Wollman, K. D. Irwin, G. C. Hilton, L. L. Dulcie, D. E. Newbury, and J. M. Martinis, J. Microsc. **188**, 196 (1997).

[68] S. Friedrich et al., IEEE Trans. Appl. Supercond. **AS-7**, 3383-3386 (1997).

[69] A. Peacock, P. Verhoeve, N. Rando, A. van Dordrecht, B. G. Taylor, C. Erd, M. A. C. Perryman, R. Venn, J. Howlett, D. J. Goldie, J. Lumley, and M. Wallis, *Single optical photon detection with a superconducting tunnel junction*, Nature **381**, 135-137, (1996).

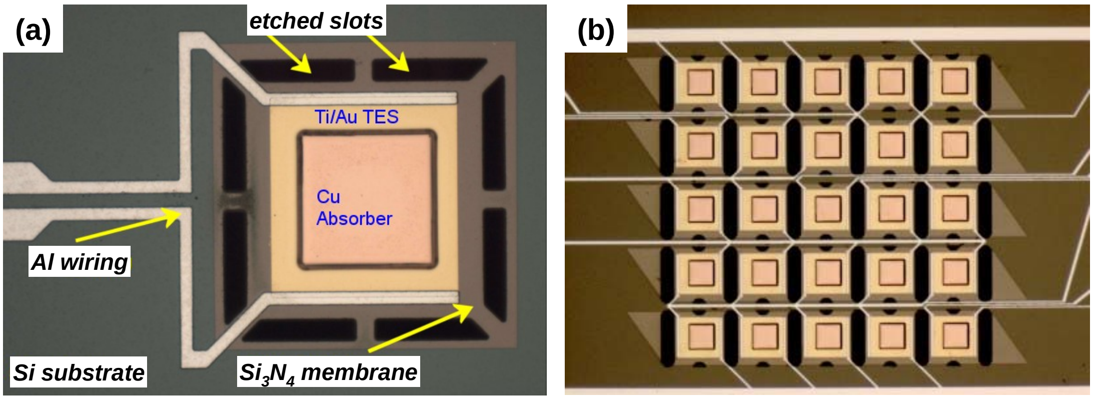

Figure 7.16: Optical micrographs of (a) a single TES and (b) a 5x5 array of TES based on Cu absorbers and Ti/Au transition-edge sensors (micrographs curtesy of SRON, The Netherlands).

absorptivity $\varepsilon \sim 1$. Note that the counting rate of the detectors is limited by the thermal time constant, which should be kept small by reducing the heat capacity of the detector.

As discussed in section 7.3.2 the energy resolution of microcalorimeters using transition edge sensors is ultimately limited by thermodynamic energy fluctuations in the detector due to the random exchange of phonons through the thermal link which connects the detector to the heat sink at temperature T_0 (phonon noise), and the Nyquist noise of the transition edge sensor. Photon noise and $1/f$ noise usually are negligible. At low temperatures in most cases the thermal noise is limiting the energy resolution. With the noise equivalent power $\mathrm{NEP} = \sqrt{4k_BT_0^2G}$ (for $\varepsilon = 1$, compare (7.3.12)) of the thermal fluctuation noise we obtain with the thermal time constant $\tau = C/G$ the energy resolution $\Delta E = \mathrm{NEP}\sqrt{\tau}$ (i.e. we set the bandwidth equal to $1/\tau$) to[70]

$$\Delta E_{\mathrm{FWHM}} \;=\; 2.355\,\sqrt{4k_BT_0^2C}\;. \tag{7.4.1}$$

Here, the factor $2.355 = 2\sqrt{2\ln 2}$ converts from one standard deviation to FWHM. As an example, for $T_0 = 0.1$ K and $C = 10^{-12}$J/K, corresponding to a detector volume of $100\,\mu\mathrm{m}^3$ for a specific heat capacity $c_v \sim 1\mathrm{J/m^3K}$, we expect $\Delta E_{\mathrm{FWHM}} \simeq 10\,\mathrm{eV}$. We see that we can improve the energy resolution by reducing T_0 and C. However, in practice this is difficult to do. Firstly, a reduction of T_0 increases the cryogenic effort in particular when going to $T < 0.1$ K. Secondly, C cannot be reduced arbitrarily by reducing the detector volume because a finite absorber volume is required to have a sufficient quantum efficiency of the detector. Thirdly, a reduction in T_0 results in a strong reduction of G (typically, due to the Kapitza boundary resistance between heat sink and sensor we have $G \propto T^3$) thereby increasing τ and hence decreasing the maximum counting rate of the detector. Therefore, one has to make a trade-off between energy resolution, cryogenic effort and counting rate. Note that the energy resolution of a detector can be derived from the NEP. For example, as already discussed in sections 7.2 and 7.3 the NEP of direct detectors and thermal detectors can be as low as $10^{-18}\mathrm{W}/\sqrt{\mathrm{Hz}}$. If such detector has a thermal time constant $\tau \simeq 1$ ms, this detector is capable of resolving an energy of a few times 10^{-19}J. This is just the energy of a soft x-ray photon with $\hbar\omega \simeq 1$ eV or a particle with the same kinetic energy.

Microcalorimeters based on transition-edge sensors (TES) positioned on Si_3N_4 membranes and using low noise SQUID preamplifier for signal amplification have been successfully fabricated and tested.

---

[70] We also can use the following intuitive argumentation: The exchange of phonons produces random fluctuations in the energy content of the absorber and consequently fluctuations in the temperature. These fluctuations can be quantified by the by using the fact that the effective number of phonons in the absorber is of the order C/k_B. The energy of a typical phonon is k_BT and the rms fluctuation of one phonon is of the order of one, therefore the mean-squared energy fluctuation in the absorber is $(k_BT)^2C/k_B$, i.e. $\langle \Delta E_{\mathrm{rms}}^2 \rangle \sim k_BT^2C$.

Usually materials with T_c well below 1 K such as Mo/Cu or Ti/Au are used. An energy resolution of a few eV at a counting rate of about 1000 counts per second at 1 keV photon energy have been reported for an effective collection area of 4 mm^2 and $T = 0.1$ K. These detectors are well suited for applications in X-ray microanalysis.[71,72,73,74] Fig. 7.16 shows optical micrographs of a single TES and an array of TES based on Cu absorbers and Ti/Au transition-edge sensors. As an example, Fig. 7.17 shows the x-ray spectrum of an ^{55}Fe source recorded by a microcalorimeter based on a Mo/Cu transition edge sensor. From the measured spectrum an energy resolution of 4.5 ± 0.1 eV FWHM at a photon energy of 5.9 keV is determined. Successive design changes improved the measured energy resolution of the sensors from 4.5 eV FWHM to 2.4 eV.[75] Sensors with this energy resolution are well matched to applications in x-ray astrophysics and terrestrial materials analysis. The best energy resolutions (at about 6 keV) obtained so far with TESs are more than 30 times better than ubiquitous silicon-lithium sensors.[76,77] Despite this impressive performance, the resolution of TESs has not yet reached the predicted theoretical limits and further improvements are expected.

Furthermore, superconducting transition-edge sensors for the wideband detection of individual photons from the mid infrared through the optical into the far ultraviolet have been fabricated.[78,79] Square-shaped ($\sim 20\,\mu\mathrm{m}^2$ on a side) tungsten transition-edge sensors have been shown to be able to detect single photon events above a threshold of 0.3 eV with an energy resolution of 0.15 eV FWHM, and with a rise and fall time of 0.5 and 60 μs, respectively. The W films have a sharp superconducting transition at about 80 mK with a transition width of less than 1 mK. The Si substrate is maintained at an operating temperature of about 40 mK, half of the W transition temperature, via the Joule heating produced by the voltage bias. The intrinsic stability of the voltage bias is due to ***negative electrothermal feedback***,[80,81] where an increase in sensor temperature and thus an increase in sensor resistance causes a decrease in Joule heating (V^2/R). Similarly, a decrease in sensor temperature causes an increase in Joule heating. This mode of operation leads to substantial improvements in resolution, linearity, dynamic range, and count rate. The improvement of the energy resolution is due to the fact that the electrothermal feedback suppresses the

---

[71] K. D. Irwin, G. C. Hilton, John M. Martinis, S. Deiker, N. Bergren, S. W. Nam, D. A. Rudman, and D. A. Wollman, *A Mo-Cu superconducting transition-edge microcalorimeter with 4.5 eV energy resolution at 6 keV*, Nucl. Instr. Meth. A **444**, 184-187 (2000).

[72] D.A. Wollman, S.W. Nam, D.E. Newbury, G.C. Hilton, K.D. Irwin, N.F. Bergren, S. Deiker, D.A. Rudman, J.M. Marinis, *Superconducting Transition-Edge-Microcalorimeter X-ray Spectrometer with 2 eV Energy Resolution at 1.5 keV*, Nucl. Instr. Meth. A **444**, 145-150 (2000).

[73] D.A. Wollman, S.W. Nam, G.C. Hilton, K.D. Irwin, N.F. Bergren, D.A. Rudman, J.M. Martinis, D.E. Newbury, *Microcalorimeter Energy-Dispersive Spectrometry Using a Low Voltage Scanning Electron Microscope*, J. Microscopy **199**, 37-44 (2000).

[74] B. Cabrera, R. M. Clarke, P. Colling, A. J. Miller, S. Nam, and R. W. Romani, *Detection of single infrared, optical, and ultraviolet photons using superconducting transition edge sensors*, Appl. Phys. Lett. **73**, 735-737 (1998).

[75] J. N. Ullom, J. A. Beall, W. B. Doriese, W. D. Duncan, L. Ferreira, G. C. Hilton, K. D. Irwin, C. D. Reintsema, and L. R. Vale, *Optimized transition-edge x-ray microcalorimeter with 2.4 eV energy resolution at 5.9 keV*, Appl. Phys. Lett. **87**, 194103 (2005).

[76] W. M. Bergmann Tiest, H. F. C. Hoevers, M. P. Bruijn, W. A. Mels, M. L. Ridder, P. A. J. de Korte, and M. E. Huber, AIP Conf. Proc. **605**, 199 (2002).

[77] C. K. Stahle, R. P. Brekosky, E. Figueroa-Feliciano, F. M. Finkbeiner, J. D. Gygax, M. J. Li, M. A. Lindeman, F. Scott Porter, and N. Tralshawala, Proc. SPIE **4140**, 367 (2000).

[78] B. Cabrera, R. Clarke, P. Colling, A. Miller, S. Nam, R. Romani, *Detection of single infrared, optical, and ultraviolet photons using superconducting transition edge sensors*, Appl. Phys. Lett. **73**, 735 (1998).

[79] J.C. Mather, *Super photon counters*, Nature **401**, 654-656 (1999).

[80] K. D. Irwin, *An application of electrothermal feedback for high resolution cryogenic particle detection*, Appl. Phys. Lett. **66**, 1998 (1995).

[81] K. D. Irwin, G. C. Hilton, D. A. Wollman, and John M. Martinis, *X-ray detection using a superconducting transition-edge sensor microcalorimeter with electrothermal feedback*, Appl. Phys. Lett. **69**, 1945-1947 (1996).

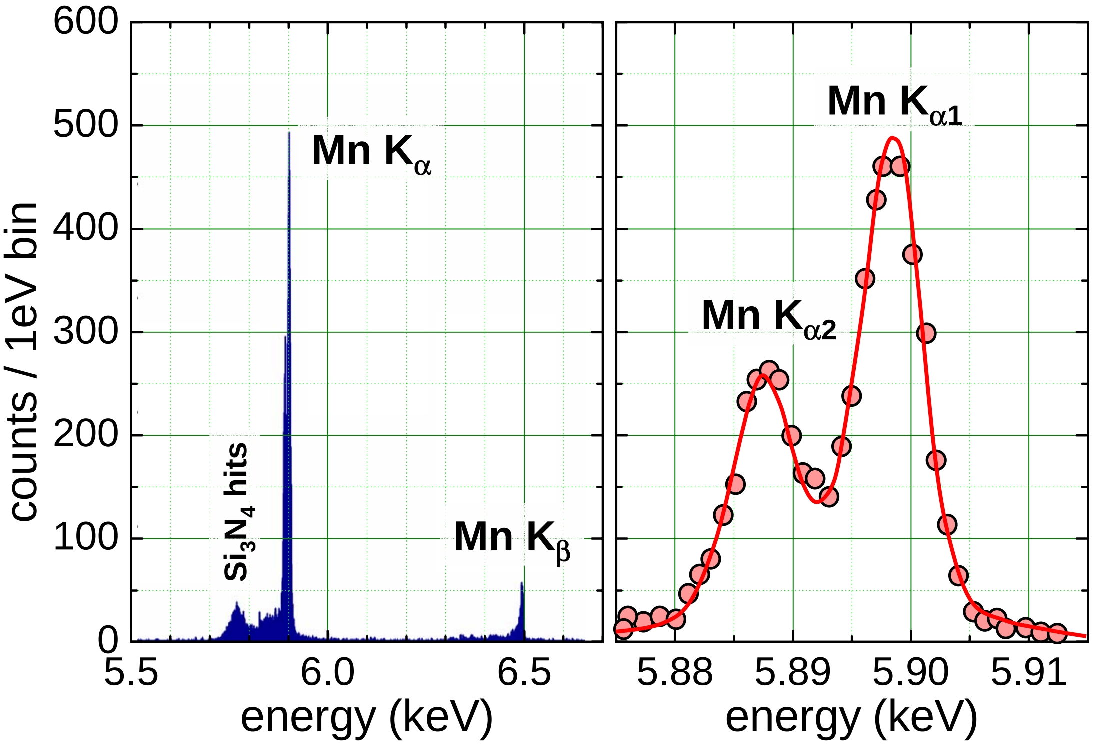

Figure 7.17: Spectrum of an ^{55}Fe source recorded by a microcalorimeter based on a Mo/Cu transition edge sensor. (a) Wide spectrum (b) a weighted least-squares fit of the Mn-K$_\alpha$ x-rays to a convolution of the theoretical line profile and a Gaussian instrument response. An instrument resolution of 4.5 ± 0.1 eV FWHM is determined (according to K.D. Irwin *et al.*, Nucl. Instr. Meth. A **444**, 184-187 (2000)).

Nyquist noise for frequencies smaller the $1/\tau_{\rm eff}$, where $\tau_{\rm eff}$ is the effective thermal time constant.[82,83,84] The achieved energy resolution of ~ 0.15 eV FWHM is within a factor of 2 of the prediction based on intrinsic thermodynamic fluctuations. The quantum efficiency (the transmission coefficient times the absorption efficiency) of the W films has not been measured directly, however, from published data a value of about 50% over the wavelength range from 1 μm to 350 nm dropping to below 10% for longer wavelengths is expected.

In order to achieve high energy resolution, the microcalorimeters have to be operated at low temperatures (typically below 0.1 K). Furthermore, the thermal conductance coupling the sensor volume to the heat sink has to be small resulting in large thermal time constants of the order of 100 μs. This limits the count rates of the microcalorimeters to a few 1000/s. These difficulties can be partly overcome by superconducting tunnel junction detectors (STJDs) discussed in the next subsection. STJDs have the potential to count at significantly higher rate because of their much faster pulse decay time. In addition, STJDs can be operated at a somewhat higher temperature of about 300-500 mK without degradation of detector performance and do not require temperature stabilization in this range. This facilitates the implementation and operation of these detectors.

---

[82] By electrothermal feedback the energy resolution is improved by a factor of about $1/\sqrt{T_0\beta}$ below what is called the thermodynamic limit ($\Delta E = \sqrt{4k_BT_0^2C}$). Here, the dimensionless quantity $T_0\beta = (T_0/R_0)(dR/dT)$ measures the sharpness of the resistive transition of the superconducting transition edge sensor.

[83] J. N. Ullom, W. B. Doriese, G. C. Hilton, J. A. Beall, S. Deiker, W. D. Duncan, L. Ferreira, K. D. Irwin, C. D. Reintsema, and L. R. Vale, *Characterization and reduction of unexplained noise in superconducting transition-edge sensors*, Appl. Phys. Lett. **84**, 4206-4208 (2004).

[84] J. C. Mather, *Bolometer noise: nonequilibrium thoery*, Appl. Opt. **21**, 1125 (1982).

7.4.2 Superconducting Tunnel Junction Photon and Particle Detectors

The first published experimental result of using superconducting tunnel junctions as particle detectors is from **Wood** and **White** in 1969, who detected 5.1 MeV α-particles from a ^{239}Pu source with a Sn/SnO$_2$/Sn tunnel junction.[85] Similar investigations were carried out by **Kurakado** and **Mazaki** about ten years later, who presented for the first time a pulse height spectrum of the α-particle energy loss in a superconducting tunnel junction.[86] Whereas in thermal photon/particle detectors the temperature increase due to an absorbed photon/particle is detected, the ***superconducting tunnel junction detectors (STDJs)*** are based on a non-thermal detection scheme. The incoming radiation generates an excess number N of quasiparticles, which is proportional to the energy E of the absorbed photon/particle. Detailed calculations for Nb show that[87,88]

$$N = \frac{E}{1.74\,\Delta} = \frac{E}{\varepsilon}\ , \qquad (7.4.2)$$

where Δ is the energy gap of the superconducting material and ε the average energy required to create a single quasiparticle. This result is quite close to $N = E/\Delta$ what is expected naively, since a minimum energy of 2Δ is required to break up a Cooper pair thereby generating two quasiparticle excitations. Of course, in reality some energy is lost into other channels what is taken into account by the factor 1.74.

In order to determine the photon/particle energy, the excess quasiparticles have to be counted within their lifetime. This can be done by measuring the increase δI of the quasiparticle tunneling current due to the generated excess quasiparticles. The integral $\int \delta I dt$ is proportional to the number N of the generated excess quasiparticles, which in turn is proportional to the energy of the absorbed photon or particle. The detection scheme of a STJD is completely analogous to a semiconductor *pn*-junction. In the latter, the absorption of a photon/particle generates electron-hole pairs which are separated in the electric field of the *pn*-junction and counted by measuring the integral of the radiation induced excess current. The operation principle of the SIS tunnel junction detector is schematically shown in Fig. 7.18. The incoming photon or particle is absorbed in the junction electrodes and generates a large number of electron and hole like excess quasiparticles by breaking up Cooper pairs. The initially highly excited quasiparticles quickly relax down to the band edge by electron-electron interaction (cf. Fig. 7.12 and related discussion). As for the semiconductor *pn*-junction these excess quasiparticles are separated via the voltage drop across the tunneling barrier and counted by measuring the time integral $\int \delta I dt$ of the excess quasiparticle tunneling current.

The electronic readout of STJDs can be provided by simple FET-based charge or current sensitive preamplifiers and conventional spectroscopy shaping amplifiers. In order to measure the electrical signal from a particle interaction, the junction is usually biased at $V < 2\Delta/e$. The signal current develops a signal voltage V_s across the parallel combination of the bias resistor R_B and the amplifier input resistance R_i in parallel with the dynamic resistance R_d of the STJD at the bias point and with the junction capacitance C_J and stray plus preamplifier input capacitance C_i (see Fig. 7.19). The signal is amplified with either a voltage- or charge-sensitive preamplifier, usually with a FET input, although a SQUID amplifier can be used instead. Note that the Josephson current is reduced to zero by applying a magnetic field parallel to the tunneling barrier.

---

[85] G.H. Wood, B.L. White, *Pulses induced in tunneling currents between superconductors by alpha-particle bombardment*, Appl. Phys. Lett. **15**, 237 (1969); Can. J. Phys. **51**, 2032 (1973).

[86] M. Kurakado and H. Mazaki, *Quasiparticle excitation in a superconducting tunnel junction by α particles*, Phys. Rev. **B 22**, 168 (1980): Nucl. Instrum. Methods **185**, 141 (1981); Nucl. Instrum. Methods **185**, 149 (1981).

[87] M. Kurakado, Nucl. Instrum. Methods Phys. Res. **196**, 275-277 (1982).

[88] N. Rando, A. Peacock, A. v. Dordrecht, C. Foden, R. Engelhardt, B. G. Taylor, P. Gare, J. Lumley, and C. Pereira, Nucl. Instrum. Methods Phys. Res. **313**, 173 (1992).

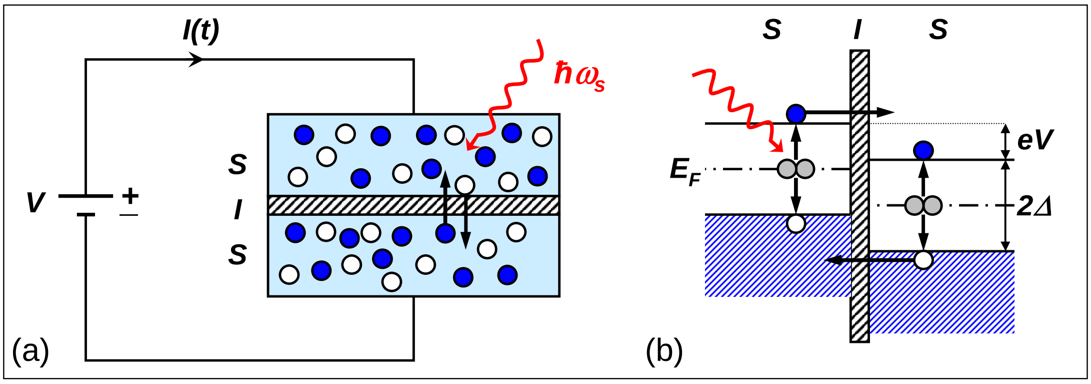

Figure 7.18: Functional principle of a superconducting tunnel junction detector. (a) A large number of electron- (full circles) and hole-like quasiparticles (open circles) are generated by breaking up Cooper pairs (shaded circles) on absorption of a photon or particle. (b) Schematic illustration of the energy diagram of a SIS junction with applied voltage V. Note that the energy of the electrons and holes is plotted up- and downwards from the Fermi level, respectively. The electron- and hole-like quasiparticles tunnel from right to left and left to right, respectively, resulting in a charge transport in the same direction.

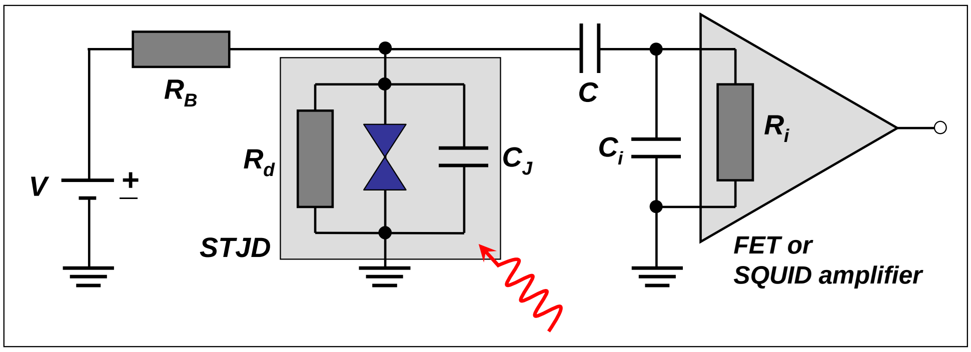

Figure 7.19: Simplified circuit diagram of a superconducting tunnel junction detector (STJD). The Josephson current through the idal Josephson element is reduced to zero by a magnetic field.

Energy Resolution

The dominating process limiting the energy resolution of STJDs is the statistical fluctuations of the number N of quasiparticles generated after the absorption of a photon or particle. The statistical fluctuation of the generated excess quasiparticle number is $\sqrt{F\,N}$, where F is the Fano factor[89] describing the statistical distribution in the number of quasiparticles. For example, for a homogeneous niobium tunnel junction, Monte Carlo simulations predict $F \simeq 0.2$. With $N = E/1.74\Delta = E/\varepsilon$ the energy resolution is given by

$$\frac{\Delta E}{E} = \frac{\sqrt{F\,N}}{N} = \sqrt{\frac{F}{N}} = \sqrt{\frac{F\,\varepsilon}{E}} \quad \text{or} \quad \Delta E_{\mathrm{FWHM}} = 2.355\,\sqrt{F\,\varepsilon\,E}\;. \tag{7.4.3}$$

Here, the factor $2.355 = 2\sqrt{2\ln 2}$ converts from one standard deviation to FWHM. There may be other factors limiting the energy resolution such as (i) an insufficient counting of the generated excess quasiparticles by tunneling, (ii) spatial inhomogeneities of the detector, (iii) diffusion losses of quasiparticle into the leads or (iv) amplifier noise. Assuming that these processes result in statistically independent fluctuations of the number of counted excess quasiparticles, the energy resolution can be written as

---

[89] U. Fano, *Ionization yield of rations: II. the fluctuations of the number of ions*, Phys. Rev. **72**, 26-29 (1947).

$$\frac{\Delta E}{E} = \frac{1}{E}\sqrt{\Delta E_{\rm intr}^2 + \Delta E_{\rm tun}^2 + \Delta E_{\rm inh}^2 + \Delta E_{\rm diff}^2 + \Delta E_{\rm ampl}^2 + \ldots} \; . \tag{7.4.4}$$

Here, $\Delta E_{\rm intr}$ is the intrinsic energy resolution given by (7.4.3).

We see that the intrinsic energy resolution increases on increasing N or, equivalently, on decreasing the average energy ε required to generate a single charge excitation. This is the basic advantage of STJDs compared to semiconductor *pn*-junction detectors. For the latter the average energy ε required for the generation of an extra electron-hole pair is given by the semiconductor energy gap E_g, which is of the order of 1 eV. In contrast, for STJDs ε is of the order of the superconducting energy gap Δ, that is typically 1 meV for most metallic superconductors. Therefore, at the same photon/particle energy, N is much larger for superconducting detectors resulting in a much better energy resolution. For comparison, the following Table summarizes the average energies required for the generation of elementary excitations in different detector systems.

detector type	***excitation***	ε
gas proportional counter	electron-hole pair	25-35 eV
scintillator	photon	≈ 3 eV
semiconductor detector	electron-hole pair	3.65 eV (Si), 2.85 eV (Ge)
STJD	quasiparticle	2.6 meV (Nb), 1.3 meV (Ta)
superfluid ^{4}He	roton	0.75 meV
superfluid ^{3}He	quasiparticle	0.14 μeV

Taking into account the statistics of the tunneling process we can rewrite (7.4.3) as

$$\Delta E_{\rm FWHM} = 2.355\sqrt{(F+F')\,\varepsilon\, E} \; . \tag{7.4.5}$$

Here we have introduced the quantity F' to account for the statistical fluctuations introduced by the tunneling process (tunneling is of course a statistical process). F' can be estimated by Monte-Carlo simulations taking into account that the quasiparticles can tunnel back and forth through the tunneling barrier several times during the lifetime. For a symmetric junction, $F' = 1 + 1/n$ is found, where n is the average number of times each quasiparticle tunnels through the barrier.[90] [91,92] As discussed

---

[90] To estimate the effect of multiple tunneling on statistical spread we assume that each quasiparticle recombines after some time t which has a probability distribution $P(t) = \tau_R^{-1}\exp(-t/\tau_R)$, where τ_R is the recombination time. During the time interval t this quasiparticle tunnels n times. We also assume that the probability distribution for n given t is Poissonian. To get the distribution for n alone, we integrate over the lifetime distribution to obtain

$$P(n) = \int_0^\infty \frac{e^{-t/\tau_R}}{\tau_R}\,\frac{e^{-t/\tau_{\rm tun}}}{n!}\left(\frac{t}{\tau_{\rm tun}}\right)^n dt = \frac{\tau_R^n\tau_{\rm tun}}{(\tau_{\rm tun}+\tau_R)^{n+1}} \; ,$$

where $\tau_{\rm tun}$ is the tunneling time discussed below. $P(n)$ has mean $\overline{n} = \tau_R/\tau_{\rm tun}$ and variance $\sigma_n^2 = \overline{n}(\overline{n}+1)$. Since the tunneling and recombination events are uncorrelated, we can add the variances of the generation and the tunneling process. For the tunneling process we obtain

$$\frac{\sqrt{N_{\rm tun}}}{N_{\rm tun}} = \frac{\sqrt{N\overline{n}(\overline{n}+1)}}{\overline{n}N} = \frac{\sqrt{N}}{N}\sqrt{1+\frac{1}{\overline{n}}} \; .$$

[91] C. A. Mears, S. E. Labov, and A. T. Barfknecht, *Energy-resolving superconducting x-ray detectors with charge amplification due to multiple quasiparticle tunneling*, Appl. Phys. Lett. **63**, 2961 (1993).

[92] D. J. Goldie, P. L. Brink, C. Patel, N. E. Booth, and G. L. Salmon, *Statistical noise due to tunneling in superconducting tunnel junction detectors*, Appl. Phys. Lett. **64**, 3169 (1994).

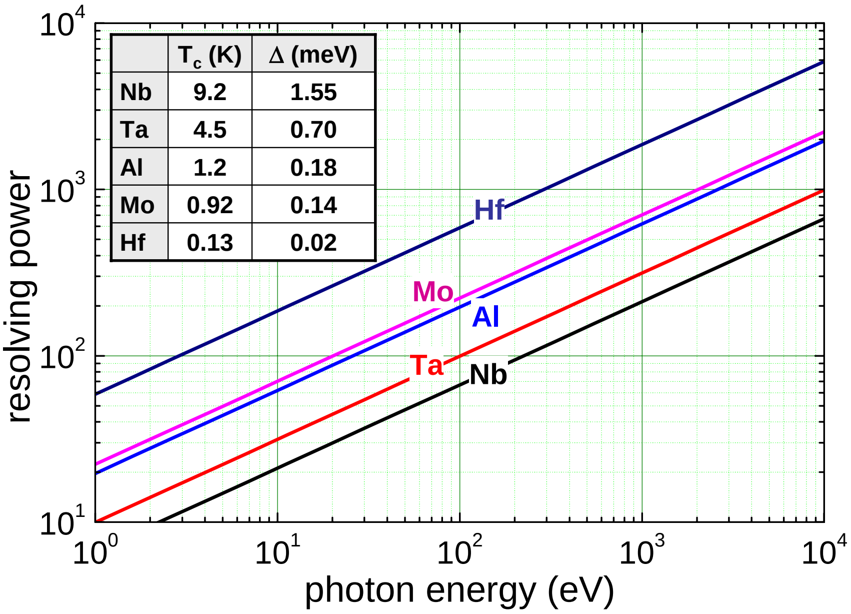

	T_c (K)	Δ (meV)
Nb	**9.2**	**1.55**
Ta	**4.5**	**0.70**
Al	**1.2**	**0.18**
Mo	**0.92**	**0.14**
Hf	**0.13**	**0.02**

Figure 7.20: Energy resolving power of STJDs fabricated from different materials. For the calculation $F + F' = 1.5$ has been used.

below, the average number n of tunneling events per quasiparticle can be estimated by dividing the observed quasiparticle lifetime by the average tunneling time, that is, by the average time it takes each quasiparticle to tunnel. Typically, $n < 5$ is realized in STJDs. Note that for $n < 1$ only a fraction of the generated quasiparticles is counted within their lifetime. In this case the energy resolution is degraded considerably by the tunneling process.

Often the energy resolving power $R = E/\Delta E$ is used. For a symmetric tunnel junction detector the energy or wavelength resolving power R limited by the statistics of charge carrier generation (Fano noise) and tunneling (tunneling noise) is given by

$$\boxed{R \;=\; \frac{1}{2.355}\sqrt{\frac{E}{(F+F')\,\varepsilon}}\;.} \tag{7.4.6}$$

This expression shows that the achievable relative spectral resolution of STJDs depends on the material of the electrodes (via ε) and other specifics of the STJD such as the tunneling time (via F'). Roughly, R is of order one part in ten to one part in a hundred in the near-UV, varying as the square root of the photon energy. Fig. 7.20 shows the resolving power of symmetric superconducting tunnel junction detectors fabricated from different materials.

By arranging a number of STJ devices into a two dimensional array, a true "three dimensional" detector can be constructed, whose output is not just the number of photons registered in each pixel of the image, but their distribution in energy throughout the UV, visible and near-IR. This unique ability to discriminate photons in wavelength without the use of filters or dispersive elements obviously comes at a price. In order to be able to distinguish the relatively feeble charges generated by the STJD above the thermal background noise, it is necessary that such devices operate at extremely low temperatures, typically below 1 K.

Quasiparticle Counting by Tunneling

Since the pioneering work by **Giaever** it is well known that the quasiparticle density can be probed by an SIS junction.[93,94] The principle of STJDs is based on the counting of the number of excess particles generated by the incident radiation via tunneling. Since insufficient counting of the generated excess quasiparticles results in a degradation of the energy resolution, the STJDs have to be designed for optimizing the quasiparticle counting process.

The main tunneling processes in a SIS tunnel junction are sketched in Fig. 7.21. Process A describes the tunneling of a quasiparticle from superconductor 1 (S1) to supercunductor 2 (S2). The probability of this process is large due to the high density of states in S1 and the large density of available empty states in S2. Process B is more complicated because it involves a Cooper pair state. In this context we emphasize that a quasiparticle excitation $|k,\sigma\rangle$, with k the momentum and σ the spin of the quasiparticle, can be electron- or hole-like with the probabilities given by the coherence factors u_k and v_k.[95] In process B a state $|k_2\uparrow\rangle$ in S2 forms a Cooper pair with a state $|-k_2\downarrow\rangle$, which is provided by tunneling. In S1 a state $|k_1\uparrow\rangle$ is left. That is, in total a quasiparticle excitation is transferred form S2 to S1, however, with the total charge e transferred from S1 to S2 due to the transfer of the involved Cooper pair from S1 to S2. Process B can be viewed as the tunneling of a hole-like excitation from S2 to S1. Process B has large probability due to the high density of states in S2 and the large density of available states in S1. The processes C and D are analogous to A and B, however, with much smaller probabilities. The existence of the two processes A and B (and the analogous processes C and D) means that tunneling in itself is not a loss mechanism. Once a quasiparticle excitation had tunneled form S1 to S2 (process A) it can tunnel back again (process B) resulting in an additional charge transfer in the same direction. This occurs for either polarity of the voltage bias. That is, in contrast to a semiconductor *pn*-junction, where the charge associated with the electron-hole pair is counted only once, in a SIS tunnel junction the quasiparticle excitation can be counted several times. As will be discussed in more detail below, the counting factor depends on the ratio of the quasiparticle lifetime and the tunneling time.

Summing up the contributions of the different tunneling processes results in the total tunneling current

$$I = \frac{1}{eR_N}\int_{-\infty}^{+\infty} \rho_1(E)\rho_2(E+eV)\,[f_1(E)-f_2(E+eV)]\;dE\;. \qquad (7.4.7)$$

Here, $f(E)$ is the Fermi function and

$$\begin{aligned} \rho(E) &= \frac{|E|}{\sqrt{E^2-\Delta^2}} && \text{for} \quad |E| \geq \Delta \\ \rho(E) &= 0 && \text{for} \quad |E| < \Delta \end{aligned} \qquad (7.4.8)$$

---

[93] I. Giaever, *Energy Gap in Superconductors Measured by Electron Tunneling*, Phys. Rev. Lett. **5**, 147 (1960).

[94] I. Giaever, *Electron tunneling and superconductivity*, Rev. Mod. Phys. **46**, 245 (1974).

[95] The quasiparticle creation and annihilation operators $\beta^+_{k\sigma}$ and $\beta_{k\sigma}$ are related to the electron creation and annihilation operators $b^+_{k\sigma}$ and $b_{k\sigma}$ via the Bogoliubov-Valentin transformations

$$\begin{aligned} b_{k\uparrow} &= u^\star_k \beta_{k\uparrow} + v_k \beta^+_{-k\downarrow} \\ b^+_{-k\downarrow} &= -v^\star_k \beta_{k\uparrow} + u_k \beta^+_{-k\downarrow}\;. \end{aligned}$$

Due to the fermionic nature of the electrons, the operators $b^+_{k\sigma}$ and $b_{k\sigma}$ have to satisfy canonical anti-commutation relations. It can be shown that the new operators $\beta^+_{k\sigma}$ and $\beta_{k\sigma}$ also satisfy the anti-commutation relations if $|u_k^2|+|v_k^2|=1$. For example, the operator $\beta^+_{-k\downarrow} = u^\star_k b^+_{-k\downarrow} + v^\star_k b_{k\uparrow}$ creates an electron in the state $|-k\downarrow\rangle$ with the amplitude $u^\star_k$ and at the same time annihilates an electron in state $|k\uparrow\rangle$ with amplitude $v^\star_k$. The calculation of the amplitudes shows that for $k \gg k_F$ we have $u_k \simeq 1, v_k \simeq 0$, i.e. here the quasiparticle excitations effectively are "electrons", whereas for $k \ll k_F$ we have $u_k \simeq 0, v_k \simeq 1$, i.e. here the quasiparticle excitations effectively are "holes".

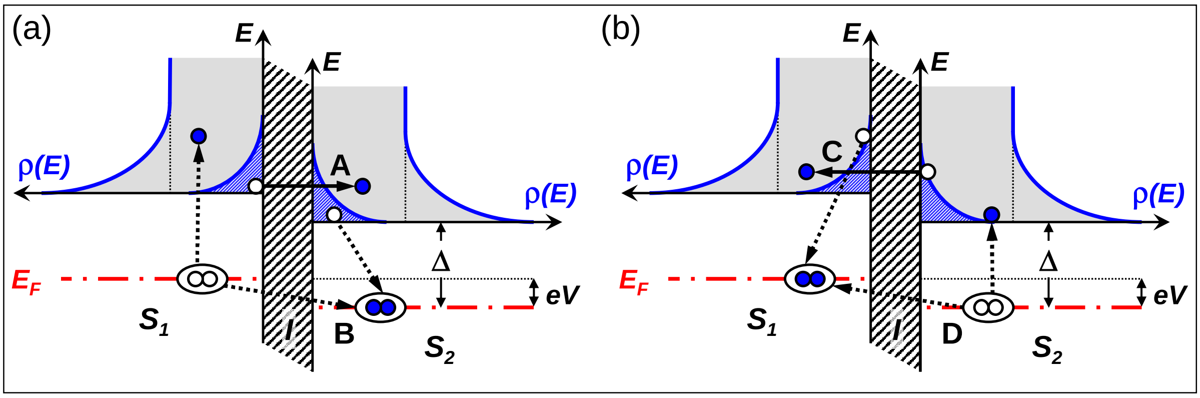

Figure 7.21: Tunneling processes in a superconducting tunnel junction. Processes A and B (a) result in charge transport from S1 to S2, whereas processes C and D (b) result in charge transport from S2 to S1. Due to the much larger probabilities of processes A and B for the chosen bias voltage a net current is obtained from S1 to S2. Processes B and D involve a Cooper pair state. They can be viewed as the tunneling of a hole-like quasiparticle excitation from S2 to S1 and vice versa, respectively. The open and full symbols mark the initial and final states, respectively.

is the normalized BCS density of states. The normal resistance R_N is related to the normal state single spin density of states n_0 at the Fermi level as

$$R_N \quad = \quad \frac{4\pi e^2}{\hbar}\,|T^2|\,n_0^2 \ . \tag{7.4.9}$$

Here, $|T^2|$ is the tunneling probability, which is determined by the thickness and height of the tunneling barrier. For $k_BT \ll |eV| < 2\Delta$ the tunneling current as function of temperature and bias voltage can be expressed as

$$I(T,V) \quad = \quad \frac{n_{\mathrm{q,th}}(T)}{2eR_N n_0}\,\rho(\Delta + eV)\ , \tag{7.4.10}$$

where

$$n_{\mathrm{q,th}}(T) \quad = \quad 4n_0 \int\limits_{\Delta_0}^{\infty} \rho(E) f(E)\, dE \; = \; 2n_0\sqrt{2\pi\Delta_0 k_B T}\ \exp\left(-\frac{\Delta_0}{k_B T}\right) \tag{7.4.11}$$

is the thermal quasiparticle density and $\Delta_0 = \Delta(T=0)$. We see that at low temperatures the thermal quasiparticle density and the associated tunneling current becomes exponentially small. For example, in a Nb tunnel junction with a volume of $(100\,\mu\mathrm{m})^2) \times 1\,\mu$m there are only about 10^6 quasiparticles at $T = 1.3$ K. This is about the same number as generated by the absorption of a 1 keV photon. That is, at low T the excess quasiparticle density generated due to the absorption of a photon/particle and the related extra tunneling current may become larger than the corresponding thermal quantities.

With the expression for the tunneling current we can write down the extra current due to the absorption of a photon/particle. For simplicity we assume a SIS junction consisting of two electrodes of the same material and the same thickness. The signal current δI_s as a function of time may be approximated by

$$\delta I_s(t) \quad = \quad \delta I_s(0)\,\mathrm{e}^{-t/\tau_D} \; = \; \frac{e\delta N}{\tau_{\mathrm{tun}}}\,\mathrm{e}^{-t/\tau_D}\ , \tag{7.4.12}$$

where $1/\tau_{\rm tun} = \Gamma_{\rm tun}$ is the tunneling rate, τ_D the decay time of the current pulse, and $\delta N = E/\varepsilon$ the excess quasiparticle number generated in the junction electrodes due to a radiation event. Although τ_D is the decay time of the current pulse, it is often called the rise time of the associated charge pulse

$$\delta Q_s(t) \;=\; \int\limits_0^t \delta I_s(t')\,dt' \;=\; \frac{e\delta N}{\tau_{\rm tun}}\,\tau_D\left[1-{\rm e}^{-t/\tau_D}\right] \; . \tag{7.4.13}$$

In first order approximation the total collected charge δQ is given by

$$\delta Q_s \;=\; e\delta N\,\frac{\tau_D}{\tau_{\rm tun}} \; . \tag{7.4.14}$$

We see that the collected charge is large, if the tunneling time is large compared to the decay time of the signal pulse.

Writing expression (7.4.10) for the tunneling current as $I = en_{\rm q,th}V/\tau_{\rm tun}$ we obtain the tunneling time[96,97]

$$\tau_{\rm tun} \;=\; \frac{2e^2 n_0\, Ad\, R_N}{\rho(\Delta + eV)} \;=\; \frac{2\pi e n_0\,\Delta\, d}{J_c\rho(\Delta+eV)} \; . \tag{7.4.15}$$

Here, we have used $V = Ad$ with A the junction area and d the thickness of the electrodes as well as $I_cR_N \simeq \pi\Delta/e$ and $I_c = J_cA$. We see that the tunneling time decreases with decreasing d and increasing J_c. For example, for Nb with $n_0 \simeq 4\times 10^{22}$/eV cm^3 we obtain a tunneling time of about 60 ns for a film thickness of $d = 10$ nm, a critical current density of $J_c = 1000$ A/cm^2 and using $\rho \simeq 1$.

Quasiparticle Lifetime: The two tunneling processes A and B of Fig. 7.21 imply that, following an interaction in say S1, leading to an increase in the tunneling process A, there will be an increase in the quasiparticle density in S2, and in turn an increase in process B. Thus, a cyclic process can occur which leads to signal amplification.[98] This process is limited by the loss rate τ_D of the quasiparticles discussed in the following. The loss rate can be expressed as

$$\Gamma_D = \frac{1}{\tau_D} \;=\; \frac{2}{\tau_R} + \frac{1}{\tau_X} \; . \tag{7.4.16}$$

The rate $1/\tau_R$ is the effective quasiparticle recombination rate and the factor of two arises because two excess quasiparticles are lost in the recombination to a Cooper pair. The factor $1/\tau_X$ includes all other loss mechanisms, for example outdiffusion of quasiparticles into the connecting leads of the junction where they are unable to tunnel. In in the ideal case they are negligible. The recombination rate depends on the quasiparticle density as[99]

$$\frac{1}{\tau_R} \;=\; n_{\rm q,th}\,\frac{1}{4n_0\Delta_0\tau_0}\left(\frac{2\Delta_0}{k_BT_c}\right)^3 \;=\; n_{\rm q,th}\,R \; . \tag{7.4.17}$$

Here, R is the recombination coefficient and τ_0 is a materials constant, which is listed in Table 7.1 together with other characteristic parameters of some relevant superconductors. Note that we can use $n_{\rm q} = n_{\rm q,th}$ in (7.4.17) only if the generated excess quasiparticle density $\delta n \ll n_{\rm q,th}$. Then we refer to the thermal

Table 7.1: Characteristic materials properties of some superconductors.

property[a,b,c]	Nb	Ta	V	Sn	Al
critical temperature T_c [K]	9.26	4.48	5.41	3.72	1.196
energy gap $2\Delta_0$ [meV]	3.05	1.5	1.6	1.15	0.34
density of states n_0 [10^{22}/cm^{3}eV]	4.06	4.08		1.45	1.56
characteristic time τ_0 [ns]	0.149	1.78		2.30	438
pair breaking time τ_B [ps]	4.2	23		110	242

---

[a] N.W. Ashcroft and N.D. Mermin, *Solid State Physics*, Holt, Rinehard and Winston International Editions, (1987).

[b] C. Kittel, *Introduction to Solid State Physics*, Oldenbourg, Munich (1983).

[c] S.B. Kaplan, C.C. Chi, D.N. Langenberg, J.J. Chang, S. Jafarey, D.J. Scalapino, *Quasiparticle and phonon lifetimes in superconductors*, Phys. Rev. **B 14**, 4854 (1976).

recombination rate. However, in STJDs this is often not the case because $n_{\mathrm{q,th}}$ becomes exponentially small at low T. For $\delta n \gg n_{\mathrm{q,th}}$ we have to use $n_{\mathrm{q}} = \delta n$ in (7.4.17) and we obtain $d\delta n/dt = \delta n/\tau_R = R\delta n^2$.

In practice the effective quasiparticle recombination rate is reduced from its intrinsic value because the phonons emitted in the recombination process can break another Cooper pairs again, thereby replacing the quasiparticles lost by recombination. The effective recombination time can be written as

$$\tau_R^{\mathrm{eff}} = \tau_R\left(1-\frac{\tau_{\mathrm{es}}}{\tau_B}\right) , \qquad (7.4.18)$$

where $1/\tau_{\mathrm{es}}$ is the escape rate of the phonons to the heat sink (e.g. the substrate) and $1/\tau_B$ is the phonon pair breaking rate. The expression in brackets is denoted as the ***phonon trapping factor***, which becomes large for $\tau_{\mathrm{es}} \gg \tau_B$. The values listed in Table 7.1 show that τ_B is in ps range for Nb or Ta and therefore is usually smaller than $\tau_{\mathrm{es}} = 4d/\gamma v_{\mathrm{ph}}$ (compare (7.3.25)), which is in the 1 ns regime for a Nb film with a typical film thickness of a few 100 nm.

Quasiparticle Trapping: In order to achieve high detection efficiency, in particular in the x-ray regime, the thickness of the junction electrodes should be as large as possible. However, in this case the tunneling time $\tau_{\mathrm{tun}} \propto d$ is increasing. According to (7.4.14) this in turn results in a reduction of the total collected charge. Evidently it is difficult to scale up the STJD to large volumes. A solution to the problem of scaling up the STJD is quasiparticle trapping.[100]

The idea of quasiparticle trapping is shown in Fig. 7.22. The superconducting junction electrodes are replaced by bilayers consisting of materials with large and small energy gap, with the low gap material adjoining the barrier. Excess quasiparticles created mainly in the thick layer of large gap material diffuse into the layer of low gap material and relax down by electron-phonon scattering. This process goes as $[(\Delta-\Delta')/\Delta']^3$ and scales with $1/\tau_0$ (see Table 7.1). The quasiparticles are trapped in the thin layer of low gap material, which forms a potential well. In this way the tunneling time, which is effectively determined by the small thickness d' of the low gap material, is significantly reduced. The magnitude of the signal current is then determined to first order by tunneling from the thin trapping layer rather than

---

[96] A.F. Cattell, A.R. Long, A.C. Hanna, and A.M. Macleod, J. Phys. F: Met. Phys. **13**, 855 (1983).

[97] Note that the tunneling time includes the dominating tunneling processes A and B. If excess quasiparticles are generated for example only in S1, process B is absent and the tunneling time is increased by a factor of 2.

[98] K.E. Gray, *A superconducting transistor*, Appl. Phys. Lett. **32**, 392 (1978).

[99] S.B. Kaplan, C.C. Chi, D.N. Langenberg, J.J. Chang, S. Jafarey, D.J. Scalapino, *Quasiparticle and phonon lifetimes in superconductors*, Phys. Rev. **B 14**, 4854 (1976).

[100] N.E. Booth, *Quasiparticle trapping and the quasiparticle multiplier*, Appl. Phys. Lett. **50**, 293 (1987).

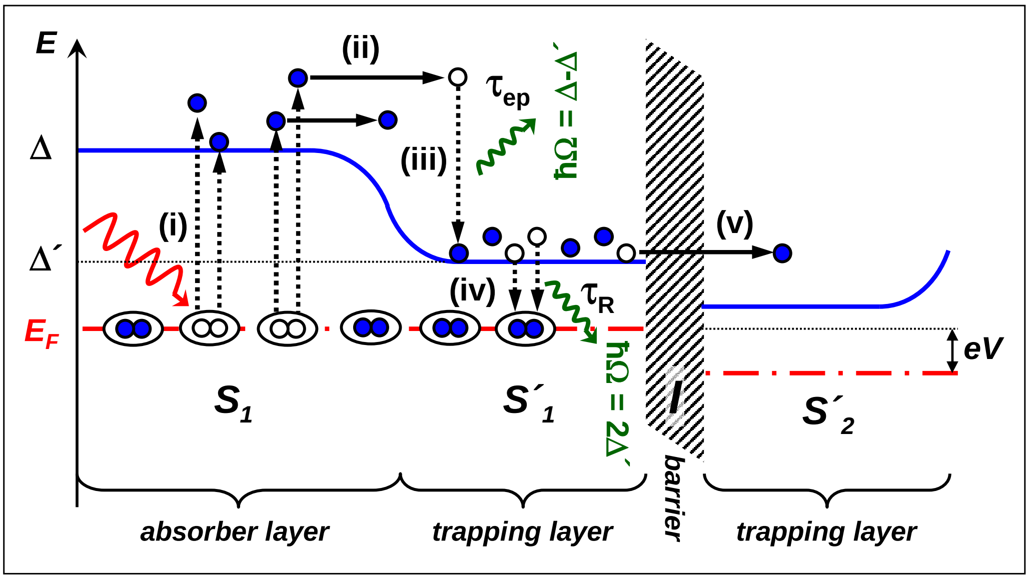
E
Δ
Δ´
E_F
(i)
(ii)
(iii)
(iv)
(v)
τ_{ep}
$\hbar\Omega = \Delta - \Delta´$
τ_R
$\hbar\Omega = 2\Delta´$
S_1
$S´_1$
I
$S´_2$
eV
barrier
absorber layer
trapping layer
trapping layer

Figure 7.22: Principle of quasiparticle trapping in superconducting tunnel junction detectors. The important processes are (i) quasiparticle generation, (ii) diffusion, (iii) relaxation by electron-phonon scattering, (iv) recombination, and (v) tunneling. In the relaxation and recombination processes phonons with energy $\hbar\Omega \leq \Delta - \Delta'$ and $\hbar\Omega = 2\Delta'$ are generated. These phonons can either escape to the heat sink or break up Copper pairs again.

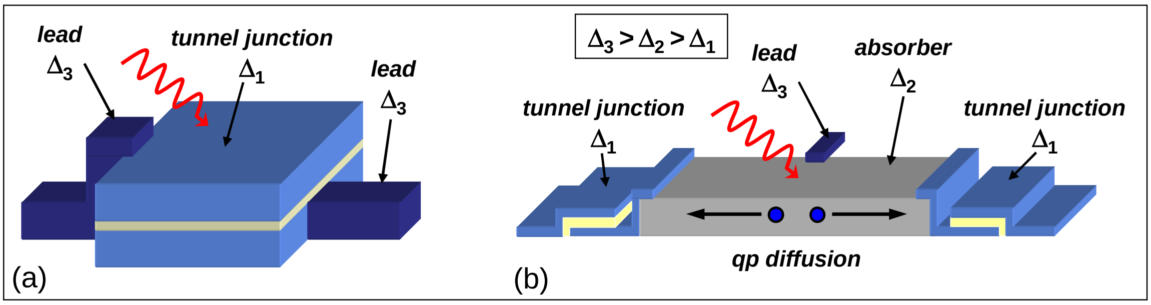
lead
Δ_3
tunnel junction
Δ_1
lead
Δ_3
(a)
$\Delta_3 > \Delta_2 > \Delta_1$
lead
Δ_3
absorber
Δ_2
tunnel junction
Δ_1
tunnel junction
Δ_1
qp diffusion
(b)

Figure 7.23: (a) STJD consisting of a low energy gap material (Δ_1, e.g. Al) contacted by leads of large energy gap material (Δ_3, e.g. Nb). (b) Detector configuration based on a medium energy gap absorber (Δ_2, e.g. Ta) and low energy gap tunnel junctions (Δ_1, e.g. Al). The absorber material is contacted by a large gap material (Δ_3, e.g. Nb) for make electrical contact to the top electrodes of the tunnel junctions.

from the thick absorber layer. That is, by employing quasiparticle trapping the total collected charge can be increased significantly thereby improving the energy resolution.

We note that quasiparticle trapping can not only be used to trap the excess quasiparticles close to the tunneling barrier but also to avoid quasiparticle diffusion into the leads. This lateral trapping can be realized by using a material with high energy gap Δ_3 for the leads of the tunnel junction made of a superconductor with $\Delta_1 < \Delta_3$ as shown in Fig. 7.23a. Another possibility is to use an absorber of medium gap material Δ_2 and couple this absorber to a tunnel junction consisting of low gap material ($\Delta_1 < \Delta_2$) as shown in Fig. 7.23b. The excess quasiparticles generates in the absorber diffuse into the lower gap junction electrodes and are trapped there. Their number is determined by tunneling. The contact to the top electrode of the tunnel junction is made via the absorber material by a high gap material ($\Delta_3 > \Delta_2 > \Delta_1$).

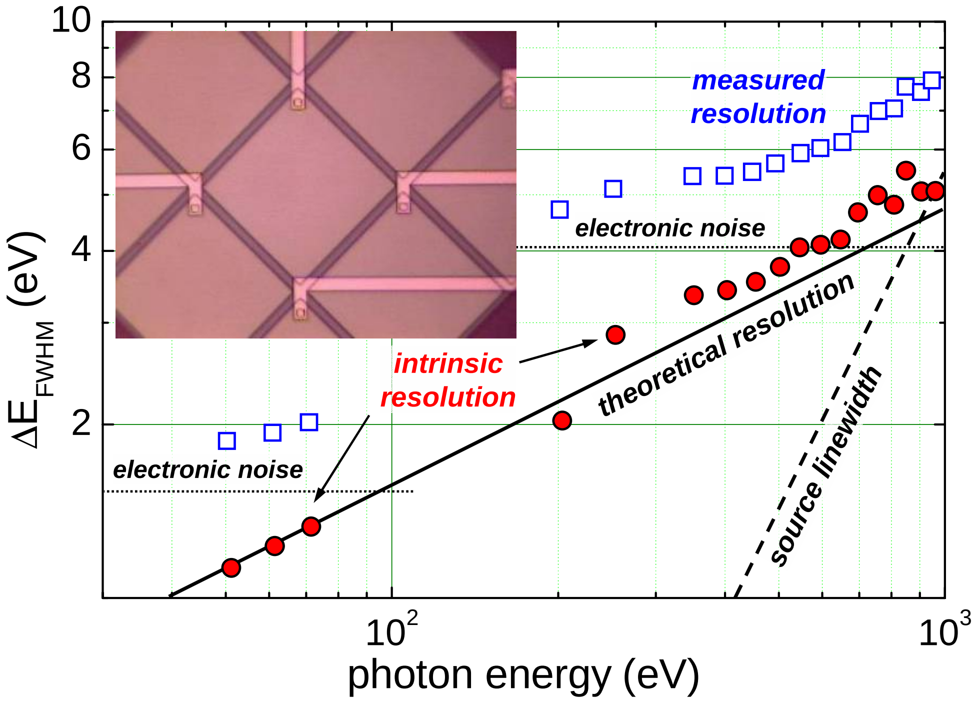

Figure 7.24: Energy resolution of a Nb/Al/AlO$_x$/Al/Nb STJD detector as a function of the photon energy. The intrinsic device resolution (full circles) is calculated by subtracting electronic noise (dotted lines) and monochromator line width (dashed line) in quadrature from the measured resolution (open squares). The solid line is the theoretical resolution limit calculated according to (7.4.5) using $F' = 1.3$. The inset shows an optical micrograph of a 3x3 detector array with a pixel size of $100 \times 100\,\mu\text{m}^2$ (according to S. Friedrich *et al.*, IEEE Trans. Appl. Supercond. **AS-9**, 3330 (1999)).

Experimental Status

At present several groups worldwide have fabricated STJDs and detector arrays for x-ray imaging and spectroscopy based on Nb/Al/AlO$_x$/Al/Nb layer structures. Here, the Al layer serves for quasiparticle trapping. For these detectors an energy resolution ranging between about 2 and 10 eV FWHM has been achieved for photon energies between about 50 and 1000 eV. The detectors can be operated at count rates as high as 10 000 counts/s per pixel. Typical operation temperatures of the detectors are 0.1 K. An optical micrograph of a 3x3 detector array and the energy resolution is shown in Fig. 7.24.[101,102]

STJDs optimized for the UV and extrem UV regime between about 20 and 200 eV based on Ta absorbers ($\Delta_2 = 700\,\mu$eV) and Al/AlO$_x$/Al tunnel junctions ($\Delta_1 = 180\,\mu$eV) have achieved a FWHM energy resolution as low as 2.15 eV, which was limited by the amplifier noise.[103] These STJDs use a lateral instead of a vertical trapping structure as sketched in Fig. 7.23b. The photons are absorber in the Ta layer and diffuse laterally into the Al tunnel junction electrode where they are trapped and counted via tunneling. Spectrometers based on STJDs already are meanwhile successfully used in many applications.[104]

---

[101] S.Friedrich, J.B. le Grand, L.J. Hiller, J. Kipp, M. Frank, S.E. Labov, S.P. Cramer, and A.T. Barfknecht, *High-Resolution Tunnel Junction Extreme Ultraviolet Detectors Limited by Quasiparticle Counting Statistics*, IEEE Trans. Appl. Supercond. **AS-9**, 3330-3333 (1999).

[102] S. Friedrich, K. Segall, M. C. Gaidis, C. M. Wilson, D. E. Prober, A. E. Szymkowiak and S. H. Moseley, *Experimental quasiparticle dynamics in a superconducting, imaging x-ray spectrometer*, Appl. Phys. Lett. **71**, 3901-3903 (1997).

[103] Ch.M. Wilson, L. Frunzio, and D.E. Prober, *Superconducting Tunnel Junction Detectors for Extreme Ultraviolet Applications*, IEEE Trans. Appl. Supercond. **AS-13**, 1120-1123 (2003).

[104] N. Rando *et al.*, *S-Cam: A cryogenic camera for optical astronomy based on superconducting tunnel junctions*, IEEE Trans. Appl. Supercond. **AS-10**, 1617-1625 (2000).

7.5 Other Detectors

To conclude the chapter on superconducting photon and particle detector we would like to mention a few superconducting detectors that are based on other detection schemes. The first one is based on an array of small grains consisting of a type-I superconductor. Each grain is much larger than the London penetration depth λ_L so that the grains stay in the Meißner state on applying a magnetic field. The temperature and magnetic field are chosen to keep the grains close to the phase boundary to the normal state. Therefore, when a particle is absorbed by a grain the deposited energy may be sufficient to switch the grain into the normal state. Switching the grain into the normal state lets the magnetic flux enter the grain. The change in flux distribution can be detected by a sensitive SQUID detector coupled to the grain. It has been shown that grains of the type-I superconductors Pb, Sn or In (typical diameter is $10\,\mu$m) can be operated in the so-called superheated state, where the applied magnetic field is slightly above the critical field without loosing the Meißner state. Such metastable state is possible, since the superconducting transition at finite field represents a first order phase transition. Then a very small energy deposition of the order of only 1 keV is sufficient to switch the small particle into the normal state. Such superheated superconducting granular detectors have been proposed in the search for weakly interacting massive particles (WIMPs) because large absorber masses can be realized.

The second detector to be mentioned is the magnetic monopole detector. Magnetic monopoles would carry the quantum of magnetic charge in the same way as electrons carry the quantum of electric charge. Our present experience is that magnetic monopoles do not exist in nature. All magnetic fields are magnetic dipoles generated by moving charges and magnetic field lines form closed loops. However, the existence of magnetic monopoles with magnetic charge quantized in units of h/e has been suggested by some elementary particle theories. If magnetic monopoles would exist, then the fundamental equations for magnetic and electric flux density, $\int \mathbf{B}\cdot d\mathbf{F} = Q_{\text{mag}}$ and $\int \mathbf{D}\cdot d\mathbf{F} = Q_{\text{el}}$, would be completely symmetrical. Here, Q_{mag} and Q_{el} are the magnetic and electric charge enclosed by a closed surface. The fact that magnetic monopoles have not yet been detected may just be related to their small number and weak interaction. A few researchers have attempted to search for magnetic monopoles using a superconducting detector. The functional principle of such detector is very simple. Suppose a monopole is passing a closed superconducting loop containing zero magnetic flux. As the monopole approaches the loop, the applied flux increases from zero to $\Phi_0 = h/2e$, i.e. half the total flux of the monopole. This will be compensated by a circulating current $I = \Phi_0/L$ in the loop with inductance L. As the monopole moves through the loop and away from it, the other half of the monopole flux causes the induced current to increase further to $I = \Phi_0/2L$ corresponding to the net flux $2\Phi_0$ in the loop. This is completely different to the interaction of a magnetic dipole with the loop. The passage of a dipole would first result in an increase and then on moving away from the loop in a decrease of the shielding current with no induced flux in the loop. That is, a sudden change of the magnetic flux enclosed by the superconducting loop in units of $\pm 2\Phi_0$ would be a clear signature for the passage of a magnetic monopole. This flux change can easily be detected by a SQUID sensor. Indeed, in early experiments a single event suggesting the passage of a monopole has been found.[105] However, this never could be reproduced later.

---

[105] B. Cabrera, *First results from a superconducting detector for moving magnetic monopoles*, Phys. Rev. Lett. **48**, 1378 (1982).